Forces and drag coefficients for cylinders in a wind tunnel

Mohamed Amine Larrifi

Dissertation submitted to the to the Escola Superior de Tecnologia e Gestão of the Instituto Politécnico de Bragança to obtain the Master Degree in Industrial Engineering in the joint double diploma with the Institut Supérieur Privé Polytechnique – Université Libre de Tunis

Supervisor
Professor Sergio Rosa

Co-Supervisor
Professor Yassine Ferchichi

Bragança, Portugal
October 2021

ACKNOWLEDGMENTS

First and foremost, I am grateful to my supervisor Sergio Rosa, not only for his huge help in this work but also for his inspiring, encouraging, and supporting personality. He was always willing to give me advice and guide me in my research. Working with him has been a great honor, and I will always consider myself lucky that I had him as an advisor. I thank him for all the help and laboratory experience provided to the development of this work, he was always willing to help, give advice and share a laugh. Also, I am grateful to my supervisor Yassine Ferchichi for his valuable help.

Working in the ESTIG lab has been a wonderful experience due to the great people in this laboratory. I am thankful to all the students that I worked with in the laboratory for making this research possible and for the great atmosphere that you created.

Of course, none of this could happen without the support and the unconditional love of my adorable family. I am grateful for my beloved mother Moufida, for giving me hope and filling me with strength in every step of this work, my great father Slim for his trust, encouragement and advices in all the steps of my life, and my sister Amira for their support and for believing in me. Thank you for being there for me, thank you for helping me to achieve my dreams.

ABSTRACT

The use of experimental resources to obtain forces and drag coefficients is increasingly applied mainly for simulating complex problems in a real way, ensuring reliable, fast and practical results, a field of interest in modern industry, especially in the automotive and aerospace industries. who want to develop projects for machines, equipment and means of transport, increasingly aerodynamic. In this context, drag forces express the total resistance of a body being traversed by a fluid in the direction of a flow. Therefore, this study proposed the simulation in a subsonic wind tunnel of the external flow in smooth cylinders, and then in rough ones, by inserting sandpaper on their surfaces. These bodies, although simple, have complex flow patterns and a high level of applicability as they are useful in real application situations, such as flow in submerged pipes and the pillars of a bridge that, in external flow, suffer the forces of drag. Thus, this work presents results of several measurements of drag on smooth cylinders, and for five different surface roughness listed as a function of their respective relative roughness $\frac{\varepsilon}{D}$. The results for cylinders without roughness are validated by comparing tables and curves of experimental drag coefficients in the literature, here taken as expected values from theoretical ones. The cylinders with roughness, on the other hand, were only presented in a qualitative comparison in relation to the values of the same model without roughness because, despite the effort to maintain stability during the reading of drag forces, the measurement system (with a resolution of 0.01 N) was greatly influenced by the presence of vibrations at high speeds causing some limitations. However, the experimental practice in the laboratory allowed to verify what was expected through the theoretical foundation of the external flows of cylinders as a function of the flow regime (Reynolds number) and the approximate behavior of the drag coefficient curves for different roughness.

Keywords: External flows, Coefficient of drag, wind tunnel, cylindrical bodies and surface roughness.

RESUMO

O uso de recursos experimentais para obtenção de forças e coeficientes de arrasto é cada vez aplicado principalmente por simularem os problemas complexos de forma real garantindo resultados confiáveis, rápidos e práticos, âmbito de interesse na indústria moderna em destaque para a automobilística e aeroespacial, indústrias estas que, desejam elaborar projetos de máquinas, equipamentos e meios de transportes, cada vez mais aerodinâmicos. Neste contexto as forças de arrasto exprimem a resistência total de um corpo sendo atravessado por um fluido na direção de um escoamento. Portanto este estudo propôs a simulação em um túnel de vento subsónico do escoamento exterior em cilindros lisos, e depois nos rugosos por meio da inserção de lixas em suas superfícies. Estes corpos, apesar de simples, possuem complexos padrões de escoamentos e uma elevada grama de aplicabilidade pois são úteis em situações reais de aplicação, como por exemplo, escoamento em canalizações submersas e os pilares de uma ponte que, em escoamento exterior, sofrem as forças de arrasto. Deste modo, este trabalho apresenta resultados de diversas medições do arrasto em cilindros lisos, e para cinco rugosidades superficiais diferentes enunciadas em função da respectiva rugosidade relativa $\frac{\varepsilon}{D}$. Os resultados para os cilindros sem rugosidade são validados por meio de comparação entre tabelas e curvas de coeficientes de arrasto experimentais da literatura, aqui tido como valores esperados aqueles teóricos. Já os cilindros com rugosidades foram apenas apresentados em comparação qualitativa em relação aos valores do mesmo modelo sem rugosidades pois, apesar do esforço em manter a estabilidade durante a leitura de forças de arrasto, o sistema de medição (com resolução de 0,01 N) foi bastante influenciado pela presença de vibrações em altas velocidades acarretando algumas limitações. Contudo, a prática experimental em laboratório permitiu constatar o que era esperado mediante a fundamentação teórica dos escoamentos exteriores de cilindros em função do regime de escoamento (número de Reynolds) e do comportamento aproximado das curvas de coeficiente de arrasto para diferentes rugosidades.

Palavras-chave: Escoamentos exteriores, Coeficiente de arrasto, túnel de vento, corpos cilíndricos e rugosidade superficiais.

INDEX

LIST OF FIGURES

LIST OF TABLES

Chapter 1

Introduction

In all specialized literature there are hundreds of studies available whose objective is to study the behavior of bodies immersed in a flow. This subject, despite presenting a very complex theory in fluid mechanics, is very important in our daily lives because it made possible the progress of the modern world in terms of machines, structures, and more efficient transport, which in the engineering context, promotes comfort human, quality of life and economic development.

Studies involving the flow of fluids over rigid bodies are of great importance in the design of several systems in the aeronautical, automotive, and naval industries, for example, whose applicability is extremely dependent on the effects of drag forces. All this relevance motivated the orientation of this work to obtain the aerodynamic drag coefficients in a practical way with the help of the experimental methodology combined with the dimensional analysis technique and the available experimental apparatus: the wind tunnel.

In general, experimental techniques enabled the evolution of manufacturing processes by designing smoother and rounded shapes, which reflects, for example, a reduction in fuel consumption. Shape details, which previously went unnoticed, can help to reduce drag and, consequently, fuel consumption. In this sense, the experimental techniques have become usual, fast and relatively economical means that do not require highly complex analytical solutions and computational mathematical modeling, because in practice the fluid itself performs the precise problem modeling.

The drag coefficient can be defined as the dimensionless number obtained in an empirical way that allows estimating the influences of shape, orientation and roughness of the body in relation to the external flow configurations for the drag forces. These coefficients are usually found for simplified elements such as flat plates, cylindrical pipes, airfoils and turbines and studied according to the Reynolds number range$C_D Re$of the flow. In view of this, in real

engineering projects the drag coefficients are standardized in technical standards books and tables.

In this context, the object of this study is to obtain drag coefficients in real cylindrical models, because even though they present a simple shape, they are usual, and with complex patterns of external flow. The high theoretical complexity of these flows does not allow for quantitative calculations without the help of experimentation, mainly because they present greater rounding and, therefore, adverse pressure gradients. In even more realistic cases, there is the influence of surface roughness, which makes the mathematical modeling and the solution of the differential equations attributed in this approach even more difficult.

1.1 Justification

The justification for studying the behavior of drag coefficients in external flows of cylindrical bodies is due to its usual application possibility, among which, some of the examples can be cited: flows over heat exchanger tubes, cylindrical rain structures, columns of bridges and towers that can have their useful life reduced once submitted to the drag caused by these flows.

1.2 Objectives

The general aim of this work was to carry out experiments to simulate real air flows over cylinders in the subsonic wind tunnel available in the Laboratory to be possible to achieve the following specific objectives:

- obtain forces and drag coefficients of cylinders for laminar flows.
- evaluate the experimental results comparing with those available in the literature.
- obtain drag forces and drag coefficients for cylinders with different surface roughness.

1.3 Methodology and Work Accomplished

This study was carried out after a previous literature review, in order to gather basic information to support the execution of experimental activities. The experimental activities took place at the Laboratory of Fluid Mechanics and Hydraulics, at the School of Technology and Management in Bragança, Portugal. After data collection, further processing of information for the preparation of tables and graphs was carried out with the aid of Microsoft Excel.

1.4 Work Organization

This work is structured in the form of chapters. Chapter 1 presented the introductory aspects, motivations, justifications and the exposition of the objectives.

Chapter 2 consists of the theoretical foundation, where the basic concepts for understanding the flows, forces, and the main components of the wind tunnel in the student context of experimental studies are presented.

Chapter 3 describes the materials and methods that make the experiments feasible. Thus, a step-by-step presentation was made with the respective figures and other pertinent considerations in the adoption of cylinders and attribution of flow regimes.

Chapter 4 presents the results of the experimental tests that will be compared using graphs and tables. Next, this information is evaluated according to the theory presented in chapter 2.

Chapter 5, in turn, closes with the concluding summary with the final considerations and suggestions for future work.

Chapter 2

Theoretical foundation

This chapter is dedicated to framing the concepts that support the theory of flows for studies in aerodynamics, emphasizing the application to submerged bodies and obtaining drag and its coefficient. As you can imagine, all this information is relevant as it makes possible the rational discussion of physical phenomena.

2.1 Basics of aerodynamics

Aerodynamics is the branch of Physics dedicated to the movement of fluids, especially air and gases, and the action of forces of different natures acting on bodies immersed in flows. In these studies, it is first worth clarifying what external flows are. These flows are those that are characterized by not occurring through a confinement, as it happens inside the pipes, being, therefore, designated as such because they happen in flow over a certain body in any way.

In all the diversity of shapes and geometries in two-dimensional flows, when there is relative movement between a body and a viscous fluid, an aerodynamic response is observed given by a resultant F_R, which can be decomposed into two components: drag F_D component of the force in the direction of movement, or parallel to the free velocity vector V_∞ and lift F_L which is oriented perpendicularly.

Said aerodynamic force is justified as a response to the combined effects of shear stress distribution τ and pressure p on the considered element. Observing in detail the effort diagram proposed in figure 1, it is worth noting that in the analysis of forces we represent:

i) an angle of attack α defined by the inclination of the body between the velocity vector current line V_∞ and the chord, c which is the distance between the leading and trailing edge;

ii) two possibilities of representation of the aerodynamic force, which, as already mentioned, parallel and perpendicular to current lines called drag and lift, or, in terms of the direction c, as perpendicular, the normal force N and the parallel as axial A.

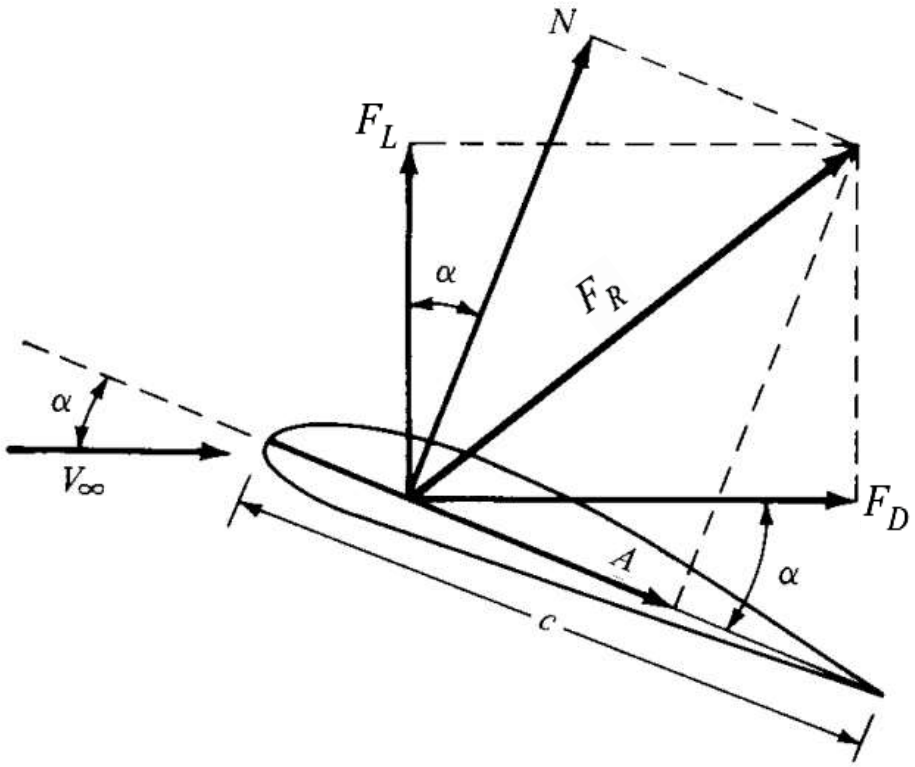

Figure 1. Generic diagram of forces on an airfoil. [1].

The angle of attack is also important because it is noted that it is the angle existing between the lift F_L and the normal force N, and between the drag F_D and the axial A forces, thus allowing to establish the mathematical relationship between these components.

$$F_L = N\cos\alpha - A\sin\alpha \quad (1)$$

$$F_D = N\sin\alpha + A\cos\alpha \quad (2)$$

At equations 1 and 2, written in terms of normal and axial force, are fully presentable when the contributions of normal pressures and shear stresses in relation to the unit span in the airfoil are determined, as per the*s* figure 2. This, a measure from the leading edge along the

upper surface to arbitrary points A and B as s_u s_l and defines functions for shear pressures p_u p_l and stresses $\tau_u \tau_l$ oriented accordingly θ.

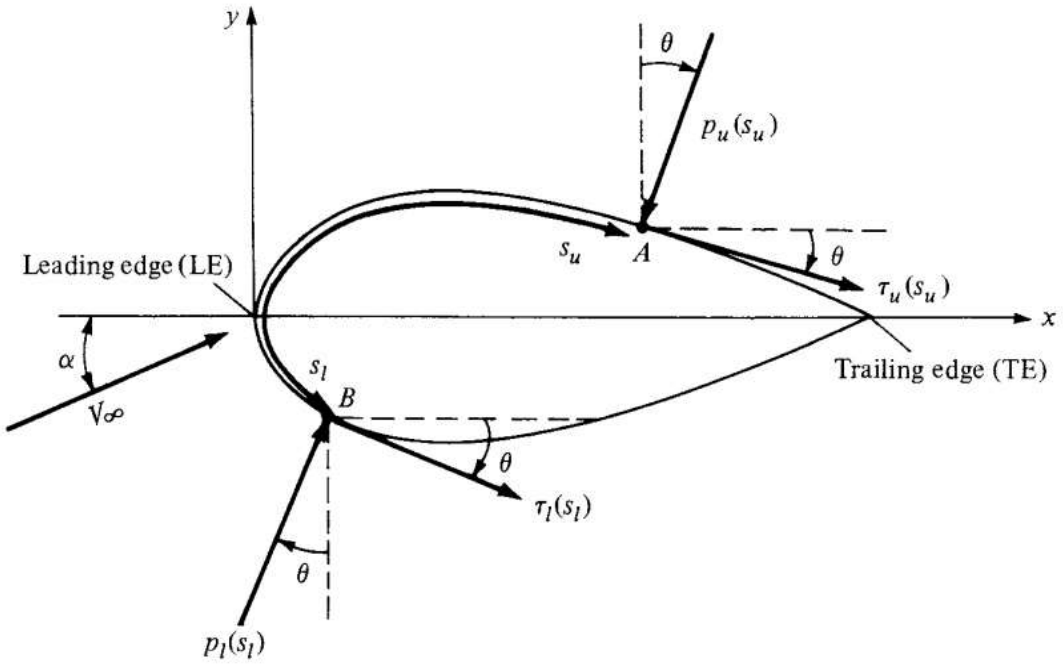

Figure 2. Element pressure and shear stress distributions [1].

The normal and axial forces per unit of elemental length given on the upper surface by N'_l e dA'_l and on the lower N'_l e dA'_l by and are the differential equations 3, 4 5, and 6. Integrating these equations with limits ranging from the leading edge to the trailing edge, we have the equations 7 and 8, which inserted in the equations 1 and 2, determine the drag and lift per unit of length.

$$dN'_u = -p_u ds_u \cos\theta - \tau_u ds_u \sin\theta \quad (3)$$

$$dA'_u = -p_u ds_u \sin\theta + \tau_u ds_u \cos\theta \quad (4)$$

$$dN'_l = p_l ds_l \cos\theta - \tau_l ds_l \sin\theta \quad (5)$$

$$dA'_l = p_l ds_l \sin\theta + \tau_l ds_l \cos\theta \quad (6)$$

$$N = -\int_{LE}^{TE} (p_u \cos\theta + \tau_u \sin\theta) ds_u + \int_{LE}^{TE} (p_l \cos\theta - \tau_l \sin\theta) ds_l \quad (7)$$

$$A' = \int_{LE}^{TE} (-p_u \sin\theta + \tau_u \cos\theta) ds_u - \int_{LE}^{TE} (p_l \sin\theta + \tau_l \cos\theta) ds_l \quad (8)$$

In a practical way, when considering the problem of determining aerodynamic forces, the equations become non-trivial and very dependent on the results obtained by computer simulation or experimental tests, which still present difficulties in presenting the real distribution of the demands $p(s)$ and $\tau(s)$ and for an approach in any bodies in an external flow.

A simplifying approach consists of the dimensional analysis technique, which, by employing the dimensional homogeneity of the flow variables, guarantees a functional relationship between dimensionless groups that is usually obtained by experimentation. However, it is first important to define the dynamic pressure as the fundamental dimensional quantity that takes into account the specific ρ_∞ mass and speed V_∞ of free flow, far enough from the body, according to the equation 9.

$$q_\infty = \frac{1}{2} \rho_\infty V_\infty^2 \quad (9)$$

The force coefficients C_L and C_D, presented in equations 10 and 11 are defined in terms of dynamic pressure by its relationship between said aerodynamic force, lift or drag, and a reference A area, assigned according to the different geometries of the body and the directions of this flow. Another relevant coefficient is the pressure coefficient C_P, and with its help it is possible to estimate the pressure distribution using information already known as the free flow pressure. p_∞

$$C_L = \frac{F_L}{q_\infty A} \quad (10)$$

$$C_D = \frac{F_D}{q_\infty A} \quad (11)$$

$$C_p = \frac{p - p_\infty}{q_\infty} \quad (12)$$

It is a consensus that the resulting aerodynamics F_R is dependent on dimensional variables involved in the flow. In these cases, the physical variables written in terms of the fundamental units of time $[t]$ [length $[l]$ and mass $[m]$ are the specific mass $[ml]$ and velocity of undisturbed flow $[lt]$, body size $[l]$, viscosity of the undisturbed fluid $[ml^{-1}t^{-1}]$, and the compressibility in terms of the undisturbed velocity of sound, $[lt^{-1}]$ which leads to $N = 6$.

$$F_R = f(\rho_\infty, V_\infty, c, \mu_\infty, a_\infty) \tag{13}$$

$$f_1(F_R, \rho_\infty, V_\infty, c, \mu_\infty, a_\infty) = 0 \tag{14}$$

By theorem of Pi Buckingham, there is a functional relationship expressed as $(N - K)$ dimensionless products called Π. By arbitrarily choosing ρ_∞, V_∞ e c, and, it has to result in the $K = 3$ equation 16, and its dimensionless products given by the equations 17,18 and 19.

$$f_2(\Pi_1, \Pi_2, \dots, \Pi_{K-N}) = 0 \tag{15}$$

$$f_2(\Pi_1, \Pi_2, \Pi_3) = 0 \tag{16}$$

$$\Pi_1 = f_3(\rho_\infty, V_\infty, c, F_R) \tag{17}$$

$$\Pi_2 = f_4(\rho_\infty, V_\infty, c, \mu_\infty) \tag{18}$$

$$\Pi_3 = f_5(\rho_\infty, V_\infty, c, a_\infty) \tag{19}$$

The theoretical development of equation 17 show Π_1 as a dimensionless product of exponents, $d = -1$, $b = -2$ and $e = -2$ revealing that it is exactly the coefficient of the resulting aerodynamic force C_R.

$$\begin{gathered} \Pi_1 = F_R \rho_\infty^d V_\infty^b c^e \\ \Pi_1 = (ml^{-3})^d (lt^{-1})^b (l)^e (mlt^{-2}) \\ \Pi_1 = \frac{F_R}{\rho_\infty V_\infty^2 c^2} = C_R \end{gathered} \tag{20}$$

Similarly, in agreement with the theorem of Pi Buckingham the development of the equation 18 reveal the product Π_2, of exponents, $h = 1$, $i = 1$ and $j = -1$, as the representation of the Reynolds number, that is, the ratio between inertial forces and viscous forces, and one of the most important parameters in fluid mechanics as it allows predicting the laminar or turbulent behavior of flows.

$$\begin{gathered} \Pi_2 = \rho_\infty V_\infty^h \, c^i \mu_\infty^j \\ \Pi_2 = (ml^{-3})^d (lt^{-1})^h (l)^i (ml^{-1}t^{-1})^j \\ \Pi_2 = \frac{\rho_\infty V_\infty \, c}{\mu_\infty} = Re \end{gathered} \tag{21}$$

Finally, working at equation 19, it can be seen Π_3, with exponentes $k = 0, r = 0$ and $s = -1$ and is the representation of the Mach number whose physical meaning is attributed as the ratio of the flow velocity to the velocity of sound, very important in the study of the effects of the compressibility of gases and liquids under high flow velocities.

$$\begin{gathered} \Pi_3 = V_\infty \rho_\infty^k \, c^r a_\infty^s \\ \Pi_3 = lt^{-1} (ml^{-3})^k (l)^r (lt^{-1})^s \\ \Pi_3 = \frac{V_\infty}{a_\infty} = Ma \end{gathered} \tag{22}$$

Making the replacements of Π_1, Π_2 and Π_3 at equation 16 the dimensional analysis is completed. Since both lift and drag are components of the net force, it is also shown that both lift and drag coefficients are completely defined as functions of dimensionless parameters.

$$f_2\left(\frac{F_R}{\rho_\infty V_\infty^2 \, c^2}, \frac{\rho_\infty V_\infty^2 \, c}{\mu_\infty}, \frac{V_\infty}{a_\infty}\right) = 0 \tag{23}$$

$$C_R = f_6(Re, Ma) \tag{24}$$

$$C_L = f_7(Re, Ma) \tag{25}$$

$$C_D = f_8(Re, Ma) \tag{26}$$

With the example of drag forces and extending the result obtained uses the equation 27 what additionally includes studies of influences of surface roughness (ε/D) on different bodies and their possible variations in the angle of attack, according to figure 3.

$$C_D = f(Re, Ma, \frac{\varepsilon}{D}, \alpha) \tag{27}$$

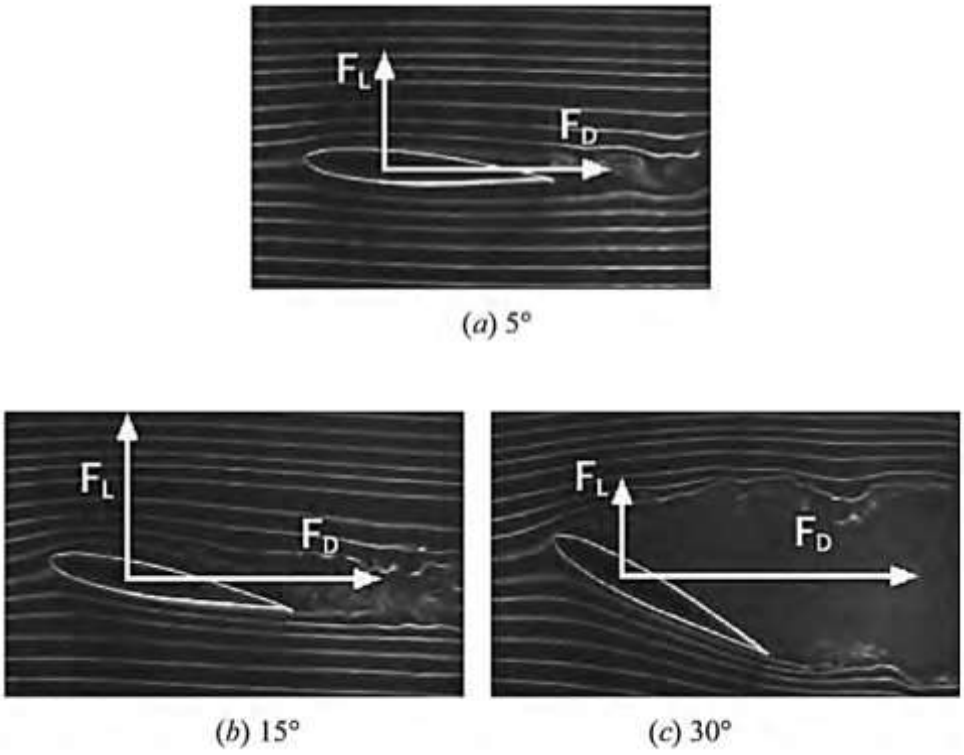

Figure 3. Aerodynamic response through three different attack angles [2].

In engineering studies, the dimensional analysis technique plays a fundamental role, proving to be quite efficient and advantageous because, in addition to reducing the amount of variables, it allows for better planning and efficiency in the search for experimental results. The technique even establishes laws of physical similarities between a smaller model and a large prototype, which saves time and financial resources.

2.2 External Flow over Cylinders

One of the main characteristics of external flows is the free growth limit of the velocity field on the surfaces of a body, which defines, therefore, the theoretical limits of a thin layer within which effects of shear forces are felt due to the viscosity of the fluid and the presence of the body. This concept, initially developed by Ludwig Prandtl, is commonly illustrated considering the external flow over flat (long) plates because this flow presents a null pressure gradient, which does not occur for most bodies.

Cylinders and spheres are included in the classification of blunt bodies, which generally have greater curvature. Once immersed in a flow, in addition to viscous actions, they present an even more significant adverse pressure gradient as the velocity increases.($V_\infty = v_e$) of this outflow. The figure 4 illustrates the kinematics of these flows, where the profile of the boundary layer and the typical phenomenon of its separation can be noted. $u(x, y)$

Boundary layer separation occurs by the deceleration of fluid particles in response to the adverse pressure gradient $\partial p/\partial x$ which gradually changes its velocity profile until, at point s, the velocity is zero. Physically, this phenomenon can be observed by the detachment of the layer from the surface, originating a reverse flow zone in the form of eddies called detachment mat according to figure 5.

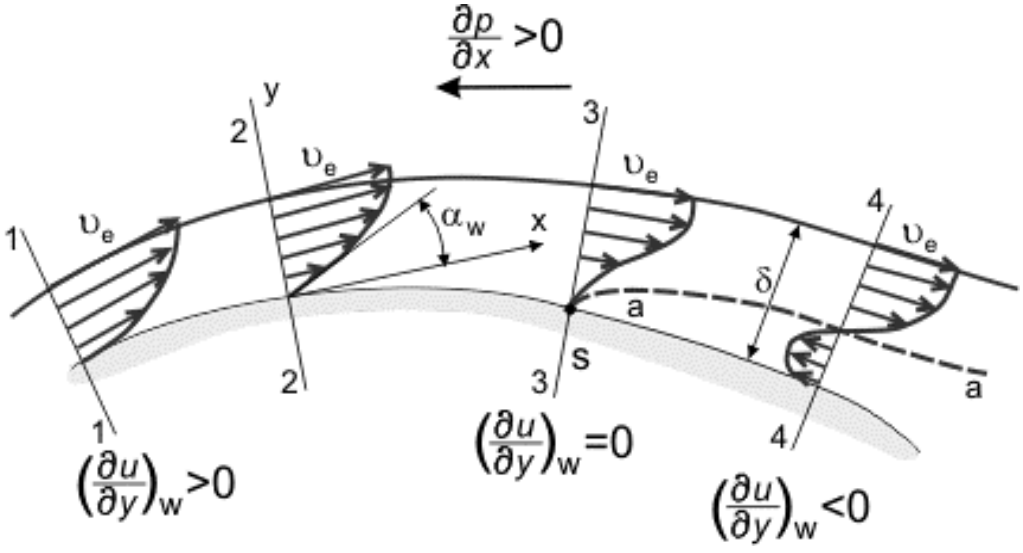

Figure 4. Velocity limit layer in curved surface body [3].

As for the flow patterns and directionality in the flows, it is observed that they can be laminar, transient and turbulent. In laminar flow, which occurs in smaller Reynolds numbers, there is flow in parallel streamlines, with little interaction between adjacent lines. As the Reynolds number increases, the flow goes through a transition until it acquires completely turbulent characteristics: randomness, circulation and the presence of eddies.

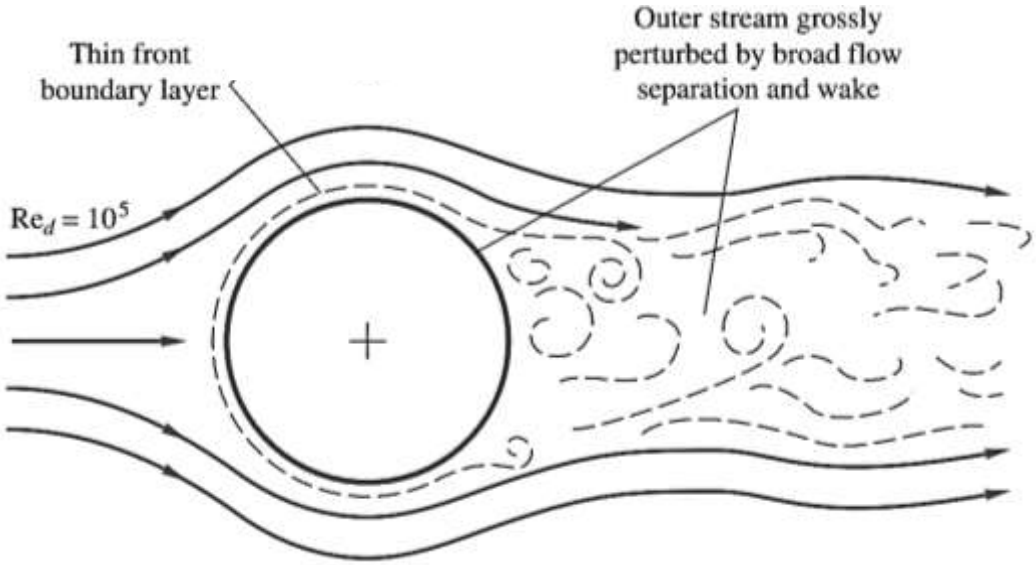

Figure 5. Actual flow around blunt bodies [4].

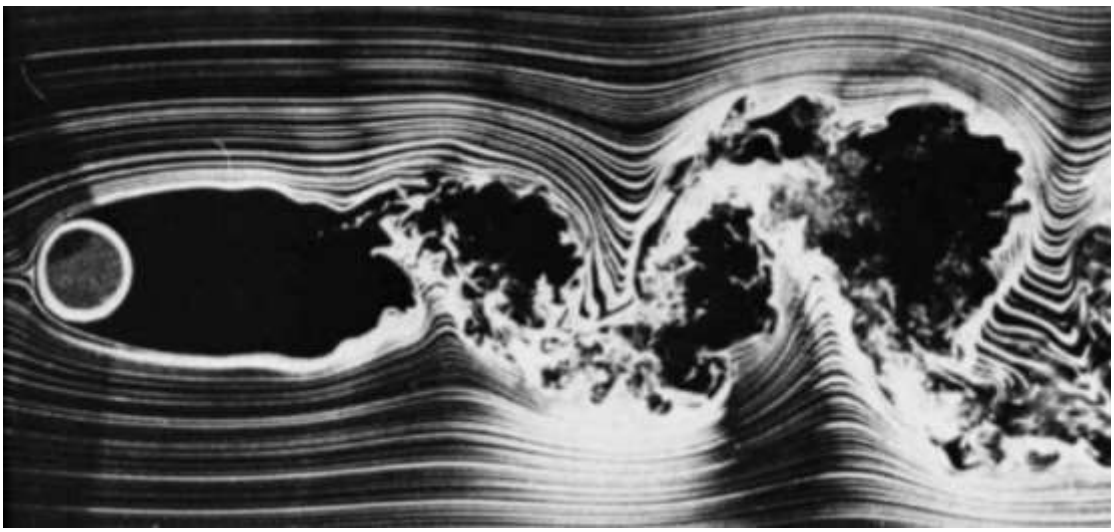

Figure 6. Laminar flow over a cylinder with $Re = 10^4$ [5].

By studying the theory of the boundary layer, it is noted that it is responsible for justifying the behavior of forces in the direction of the flow. This commitment, related by the dimensional analysis, determines the behavior of the drag coefficients through the different flow regimes that, according to the figure 7, is the experimental curve of the incompressible cross-flow $(Ma \leq 0{,}4)$ over an infinitely long and smooth cylinder.

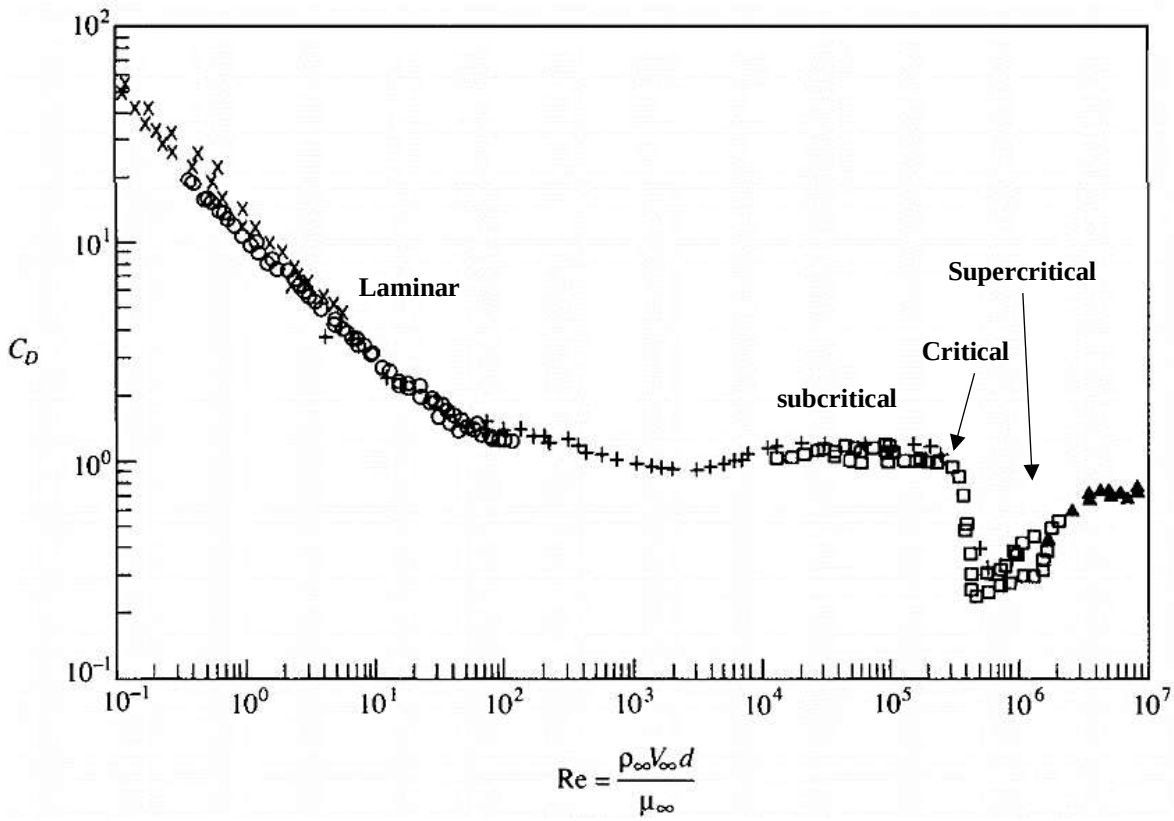

Figure 7. Experimental result of drag coefficient in cylinder for $C_D = f(Re)$ [1].

As you can see, there are some regions of the curve that are worth mentioning. In what is known as Stokes flow, interval $0 < Re < 5$ there is a preponderance of viscous effects with a balance of pressure and friction forces, revealing a decrease in the drag coefficient as the Reynolds number increases.

When, $5 < Re < 40$, the boundary layer surrounds the surface with no separation from the boundary layer, although stable eddies and vortices can be seen, a region separated from the flow at the rear of the cylinder illustrated by figure 8.

Figure 8. Laminar flow over a cylinder with $Re = 26$ [1].

As the number of Reynolds increases above $Re = 40$ the flow at the rear of the cylinder becomes unstable due to the asymmetry of vortex distribution and the effects of pressure differences between the faces of the body. At the rear, there is the presence of a turbulent mat and there is a reduction in the drag coefficient up to $Re = 5\ x\ 10^3$ limit by which the largest portion of the drag (around 95%) is due to the effects of pressure.

Later, in the track, $5\ x\ 10^3 < Re < 10^5$ the subcritical regime takes place, in turn marked by the presence of the Von Karman treadmill, on the rear face, visibly unstable and wide. In this region, by figure 7, the high and relatively constant drag coefficient can be seen in $C_D = 1{,}2$, a behavior also observed in other blunt bodies.

In the critical range, at some point between $10^5 \leq Re \leq 4\ x\ 10^5$, usually $Re = \ 2\ x\ 10^5$ the phenomenon of layer separation occurs. The drag crisis is clearly noticed, which results in an abrupt drop in the coefficient value (mainly the pressure portion) with $C_D = 0{,}3$ an apparent decrease in the size of the turbulent wake.

Said reduction in the turbulent mat is due to the displacement of the separation point from $\theta_s \approx 80^0$ when the layer is laminar, to a point further away from the surface as it becomes turbulent. The turbulent layer is more resistant to the adverse pressure gradient with greater adhesion to the surface, and therefore its separation is delayed by approximately $\theta = 120^0$. The figure 9 shows the fluid-surface interaction and the separation point measurement.

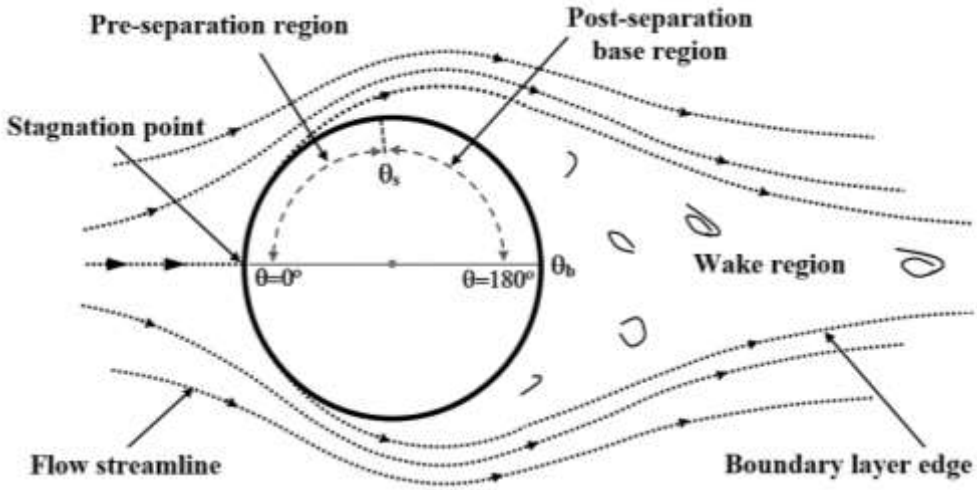

Figure 9. Measurement of the flow separation angle [7].

Related to the study of the separation point, experimental results such as those presented in figure 10, show that the presence of surface roughness in cylinders is extremely significant, especially in the flow transition. Essentially, turbulence induction occurs in which the boundary layer is delayed beyond $\theta_s \approx 80^0$, as discussed. By increasing the degree of surface roughness in a cylinder of the same diameter D, the drag crisis is anticipated for lower Reynolds numbers and visibly results in a decrease in the size of the turbulent wake.

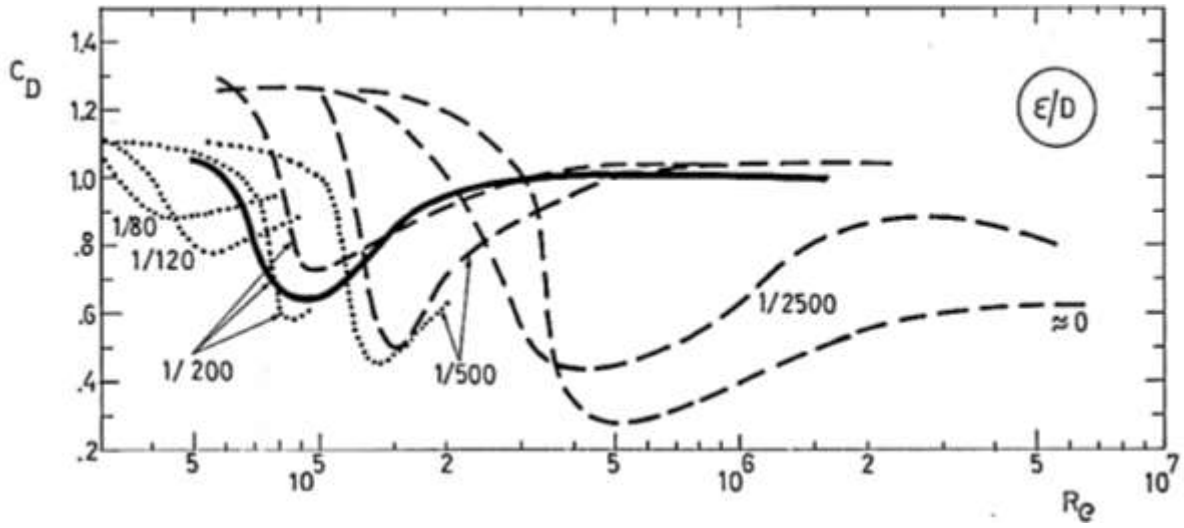

Figure 10. Experimental result of the drag coefficient crisis in cylinders when

$C_D = f(Re, \varepsilon/D)$ [8].

Finally, in the supercritical range of figure 7 measured by the interval, ($4\ x\ 10^5 < Re < 6\ x\ 10^6$ the drag coefficient increases, and the flow characteristics are uncertain, however it is known that the boundary layer is turbulent and with practically zero viscous stresses. For the same cylinder by inserting roughness, the Miller and Wong experiment (Figure 11) agree that in that region, there are no significant variations in the drag coefficient.

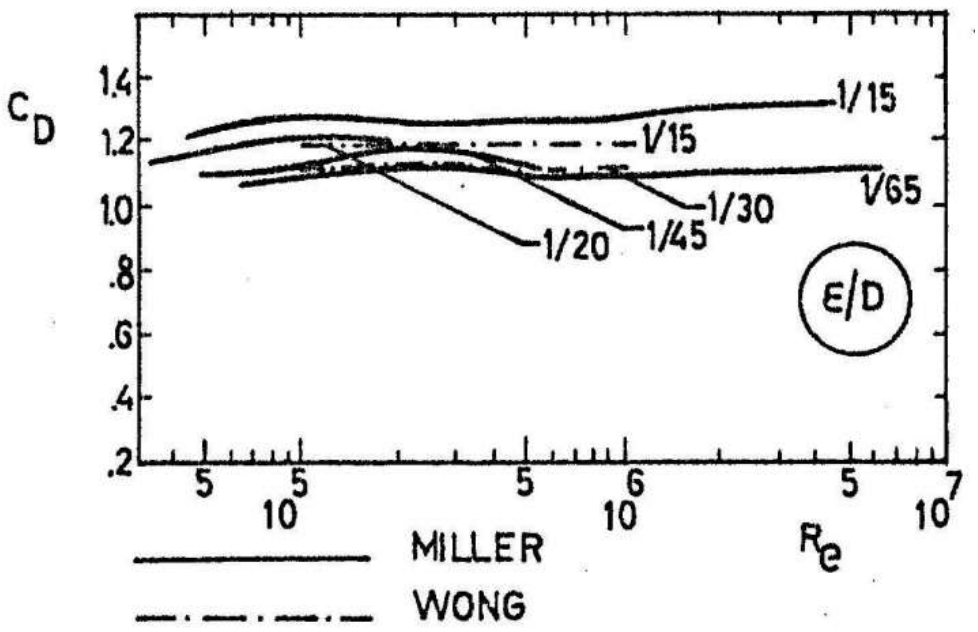

Figure 11. Drag coefficient in post-crisis cylinders when $C_D = f(Re, \varepsilon/D)$ [8].

2.3 Drag coefficient of other geometries

In geometries of practical interest, drag coefficients usually depend on the Reynolds number especially when they are less than $Re = 10^4$ however, above this value, and for most geometries, drag coefficients are constant and can be easily obtained from tables of figures 12 and 14 for two-dimensional and three-dimensional bodies experimentally.

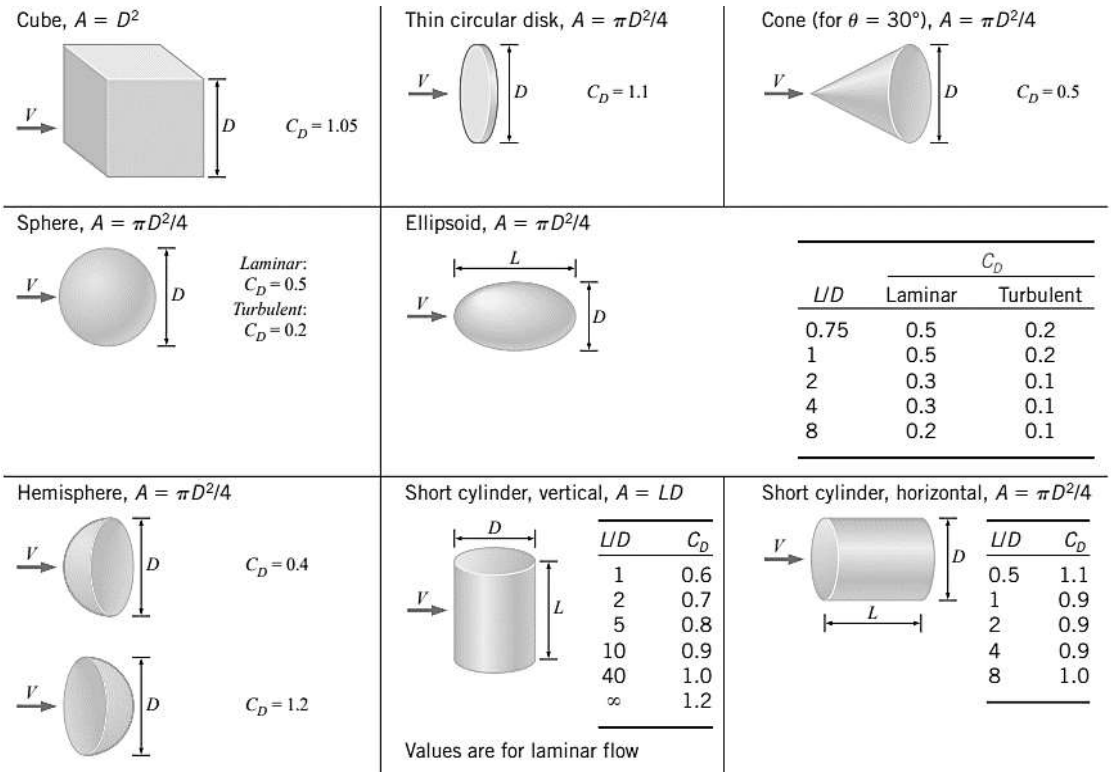

Figure 12. Drag coefficients for three-dimensional bodies in $Re > 10^4$ based on the front area [2].

From the tables, it is observed that the body's orientation in relation to the flow, and the body shape are some of the main influencing factors. An example can be seen by the figure 13, the flat plate in two configurations, one parallel to the flow, which has the preponderant friction drag, and the perpendicular where the pressure drag dominates. Through these configurations, the drag coefficient is smaller for a parallel plate and higher for a perpendicular plate because of the separation of the flow that increases the pressure difference.

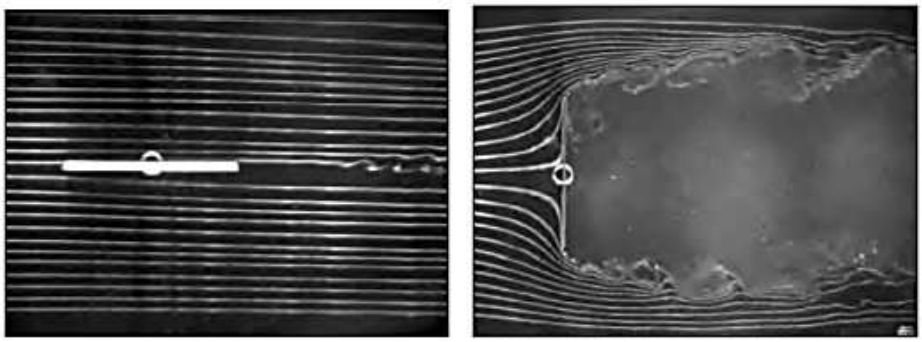

Figure 13. Different configurations of flat plate flow [2].

Details relating to body edges can also cause significant variations in the value of the drag coefficient. From the figure it can be seen that rounded edges reduce the drag coefficient, which is also the fairing principle used for the development of aerodynamic bodies.

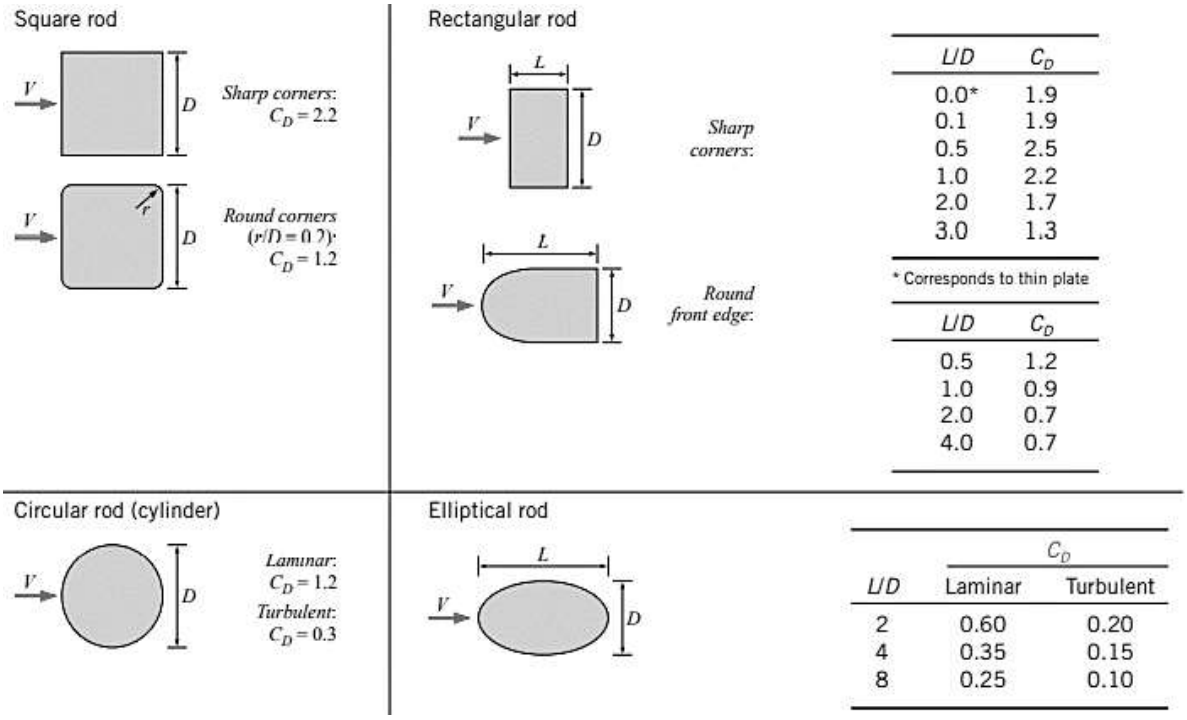

L/D	C_D
0.0*	1.9
0.1	1.9
0.5	2.5
1.0	2.2
2.0	1.7
3.0	1.3

* Corresponds to thin plate

L/D	C_D
0.5	1.2
1.0	0.9
2.0	0.7
4.0	0.7

L/D	C_D Laminar	C_D Turbulent
2	0.60	0.20
4	0.35	0.15
8	0.25	0.10

Figure 14. Drag coefficients for two-dimensional bodies in $Re > 10^4$ based on the front area [2].

In low Reynolds numbers, the acceleration elements of Navier Stokes' equations of motion can be neglected. Thus, simple geometries such as spheres have well-defined solutions, which allows analytically estimating their drag coefficient by Stokes' Law, the equation of drag F_D on a sphere $Re < 1$

$$C_D = \frac{24}{Re} \tag{28}$$

$$F_D = 3\pi\mu VD \tag{29}$$

2.4 Experimentation in Wind Tunnel

Generally speaking, studies of flows are commonly carried out combining theory and experimental techniques given the complexity of the equations of motion, presence of viscous terms and the variety of geometries. This, the experimentation consists in the application of dimensional analysis and modern equipment such as wind tunnels, which are very important for understanding real flows.

Figure 15. Submarine model in test section in the wind tunnel [2].

The wind tunnel consists of an experimental apparatus that uses the principle of relative movement between fluid and bodies in your test section. Due to their diversity, these equipments receive generic classifications usually according to the flow velocity and their geometrical configuration [11].

The classification in terms of flow velocity takes into account the Mach number. At low speeds, the tunnel is called subsonic $(Ma < 0{,}8)$ and these are widely used for student purposes. Transonic tunnels are those that operate in the vicinity of $Ma = 1$, the most common in the aeronautical industry. When the compressibility effects are even greater, supersonic tunnels $(1 < Ma < 5)$ are used in studies of jet turbines and hypersonic tunnels for even higher Mach numbers, as in the case of studies in rockets and spacecraft, for example.

In subsonic tunnels the specific mass of air is approximately constant and the presence of a contraction before the test section causes an increase in velocity and a decrease in pressure to occur. Under these conditions, the opposite occurs for supersonic tunnels that, because of the increase in compressibility, have their test section after a diffuser so that the pressure decreases and provides the highest possible speed in the test region.

These conclusions are obtained from the mass and momentum conservation equations and an isentropic relationship [12], which lead to equation 33. For that reason, an increase in the area causes a decrease in velocity V when the flow is subsonic $(Ma < 1)$ and an increase in velocity when it is supersonic.$(Ma > 1)$

$$\dot{m} = \rho . V . A$$

$$\frac{d\rho}{\rho} + \frac{dV}{V} + \frac{dA}{A} = 0 \tag{30}$$

$$\rho V dV = -dp \tag{31}$$

$$dp = \left(\frac{V}{Ma}\right)^2 d\rho \tag{32}$$

$$(1 - Ma^2)\ \frac{dV}{V} = -\frac{dA}{A} \tag{33}$$

In a simplified context, taking a subsonic wind tunnel, according to the geometric configuration, these configure two circulation paths: open and closed circuit. In an open circuit, recirculation of the air flow occurs through a suction fan that directs the air outwards and restarts the process in the tunnel entrance element, as illustrated in figure 16. Similarly, the figure 17 shows the recirculation to the closed-loop tunnel that takes place by the aid of rotating return vanes.

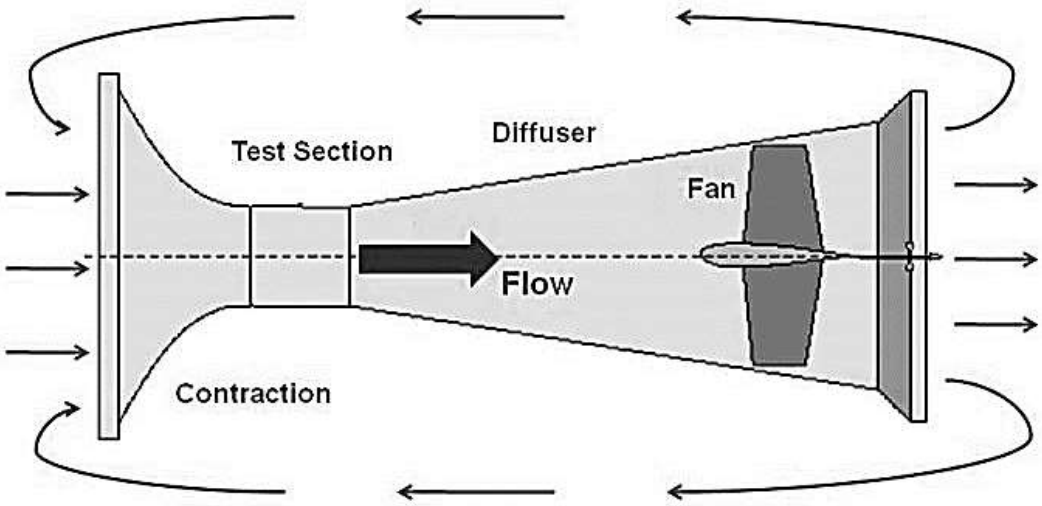

Figure 16. Open-circuit wind tunnel [13].

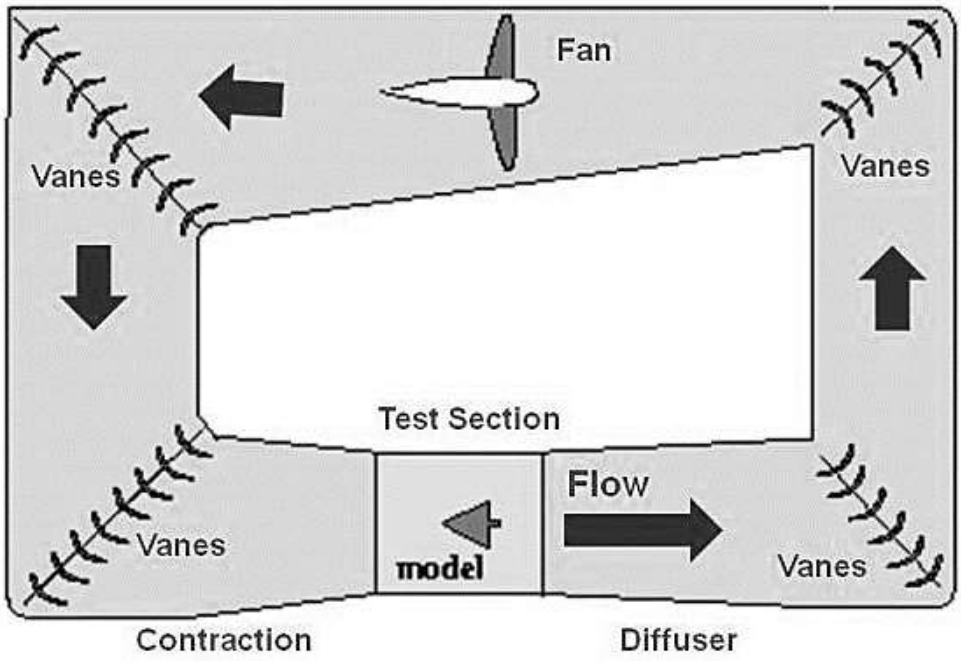

Figure 17. Closed loop wind tunnel. [14].

The elementary components of a simple wind tunnel are contraction and stabilization chamber, test section, diffuser and propulsion system sized as a function of the required speed, purpose of the test and dimensions of the body to be studied, thus defining the design of the tunnel that can often assume large proportions.

Figure 18. Gigantic wind tunnel at NASA's Ames National Aerodynamic Complex, Moffett Field, United States [15].

Figure 19. Car in the test section of an automotive wind tunnel at the Aerodynamic Test Center of BMW in Munich Germany [10].

Taking an open circuit subsonic wind tunnel, it is observed that the contraction cone is the first major element of the design, and just before its entrance is the stabilization chamber. This chamber is composed of screens with meshes in the form of a honeycomb that direct, even out and reduce the turbulence of the inlet flow, which in turn is forced through the contraction so that the increase in speed occurs, which can be observed by the continuity equation.

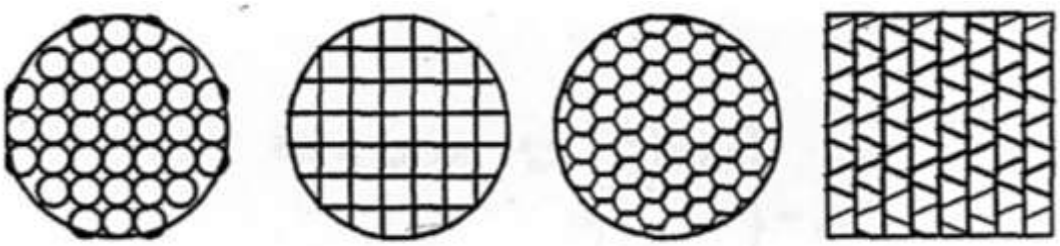

Figure 20. Different mesh geometries for the stabilization chamber [11].

The test section is the body positioning location, which is in turn connected to measurement systems such as sensors and scales that allow obtaining aerodynamic forces and simulating a real or dynamically similar flow. Basically, this section should be long enough so that disturbances resulting from shrinkage and screens are dampened without causing boundary layer growth and energy losses. The walls must be such as to facilitate the handling of the experiment without interference, and do not disturb the flow.

The diffuser, located right after the test section, is the element very sensitive to design errors and acts by decelerating the air flow as its area increases towards the outlet. This process is intended to take place over a short distance and with as little energy loss as possible which leads to greater design savings, better performance and efficiency.

Finally, the propulsion system has the presence of the fan (axial or centrifugal) responsible for the formation of the air flow by an increase in pressure H with conditions to drain at a flow rate Q. The usual ones are the axial suction fans, those that create the flow from inside to outside the tunnel, although some installations are made with inlet fans known as blowers, however, in these conditions, there is greater turbulence and less control of the flow inside the tunnel. tunnel.

The basic sizing of a fan takes into account the energy losses in each tunnel component. However, commercial catalogs are based on fan power given by the equation 34 it's the value of is the specific gravity of the air γ. Power factor η is the relation between useful power acquired by the fluid N_u and the motive power supplied by the motor N_m to its axis, important for the selection of its rotor [17].

$$N_m = \gamma . Q . H_m = \frac{\gamma . Q . H_u}{\eta} \tag{34}$$

2.5 Computational Fluid Dynamics

The computational fluid dynamics (CFD - Computation Fluid Dynamics) allows, through algorithms, the study and solutions of differential equations that model the real flow, making the handling of minutely important factors in wind tunnel tests faster. For this, the CFD is performed through the steps of pre-processing, resolution and post-processing [18].

Pre-processing consists of defining the input data of a problem that include definition of the computational domain, generation of the grid (a grid of cells, control volumes or elements), selection of the pertinent physical and chemical phenomena, fluid properties and assignment of boundary conditions.

During the resolution phase, there is Integration of the conservation equations of mass, momentum and energy over the finite control volumes of the domain, and the conversion of integral equations into a system of algebraic equations, and the solution of algebraic equations by an iterative method.

The solution is defined in nodes within cells with precision governed by the number of cells in the grid. The greater the number of cells, the better the accuracy of the solution, and both the accuracy of a solution and its cost in terms of hardware and computation time depend on the accuracy of the grid.

Finally, post-processing includes visualizing the domain and mesh geometry, plotting vectors as well as surfaces, volumes, manipulating the visualization (translation, rotation,

scaling, etc.) and obtaining the pertinent information in dynamic results display and or graphics like the figures 21 and 22. These figures show results of variation of speeds and external flow pressure on a cylinder with a radius equal to 50 mm and a length of 100 mm using the SOLIDWORKS Flow Simulation software.

When examining the information from the figure 21 on the left, the blue coloring shows that the velocity is indeed zero at the stagnation point, green on its outlines and yellow for flow velocity V_{∞}. On the right side, the blue coloration close to the rear surface indicates points of null velocity where it is observed in the color changes (dark blue to light greenish blue) the speed variations, which reveals the turbulent nature of the belt. The figure 22 confirms that pressure is maximum at the point where velocity is minimum, and minimum where velocity is maximum.

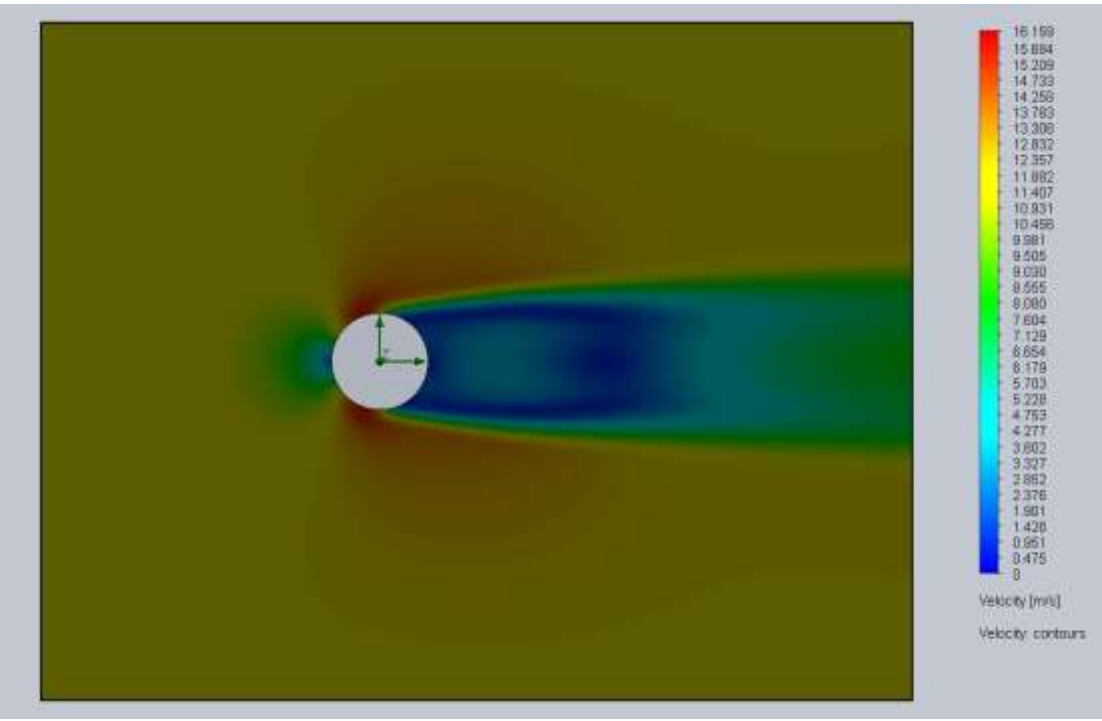

Figure 21. Cylinder speed variation when $Re = 40.607$ [20].

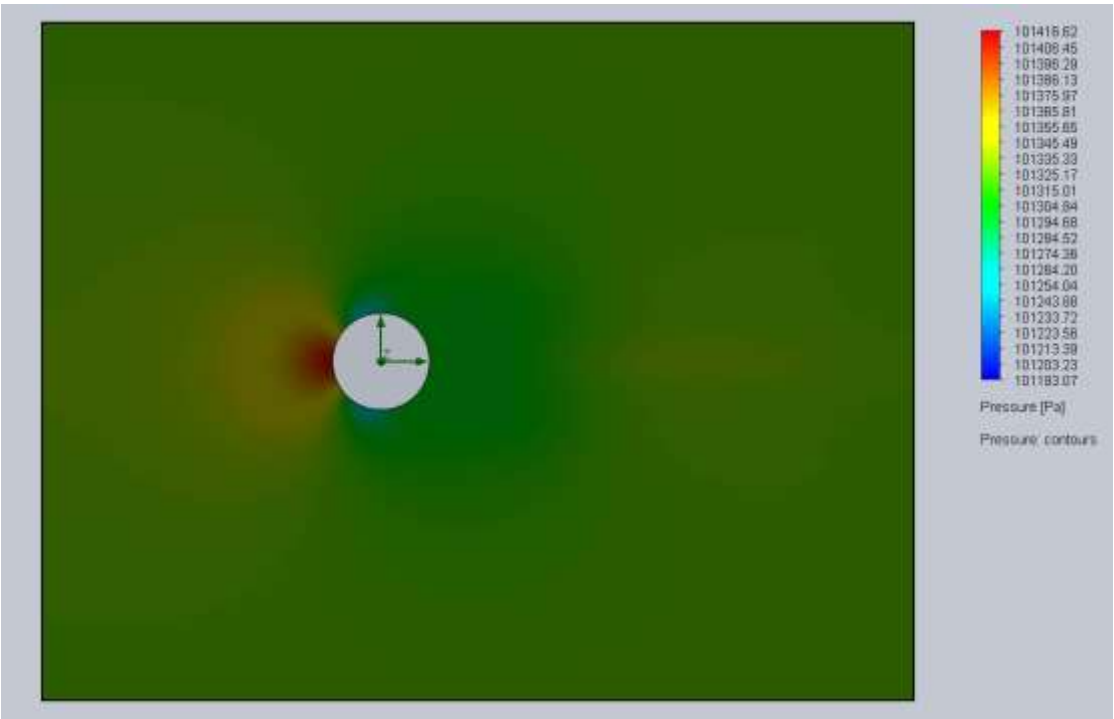

Figure 22. Cylinder pressure variation when $Re = 40.607$ [20].

Chapter 3

Materials and Methods

This chapter presents the materials and methods that enabled the proposed experimental study. Thus, the following topics show the adoption of cylinders and roughness for the simulations, description of the experimental apparatus, and other procedures in the script, thus allowing the simulation of external flows to obtain drag forces. After that, it is possible to compare the results with those available in the literature and carry out the validation of the technique.

3.1 Definition of materials

Primary, the definition of materials took into account the availability of drag coefficients already known in the literature for smooth cylindrical elements of constant cross section diameters D and lenghts$L$immersed in an external flow. In the moderate range $10^3 < Re < 10^5$ the coefficients are essentially constant and tabulated according to the dimensionless relation L/D.

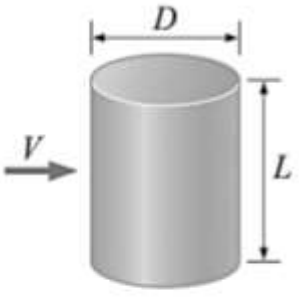

L/D	C_D
1	0.6
2	0.7
5	0.8
10	0.9
40	1.0
∞	1.2

Figure 23. Constant drag coefficients for smooth cylinders with different L/D [2].

In this context, table 1 presents the selected dimensions for the cylindrical elements i_n, which is the reference index for identifying each cylinder under study.

Table 1. Dimension of the cylinders.

Dimensions	**Cylinder i_n**		
	i_1	i_2	i_3
Characteristic measure D	$0{,}04\ m$	$0{,}04\ m$	$0{,}04\ m$
Length L	$0{,}15\ m$	$0{,}10\ m$	$0{,}05\ m$
Reletionship L/D	3,75	2,50	1,25

The second step consisted of gluing abrasive sheets (negligible thickness) on the outer surface of each cylinder to study the effects of surface roughness on forces and drag coefficients under the same the flow condition. In these abrasive sheets, the absolute roughness will be the values of the standardized estimate of the average grain sizes and are informed by commercial tables.

The commercial designation of abrasive sheets is given according to particle size. On a grain scale ranging from coarse ones, P40 is the one with highly coarse and P1000 the lowest. 5 sheets of different grain sizes were selected, which are displayed together with their respective absolute roughness in table 2 and can be visualized in the successive figures.

Table 2. Selection of abrasive sheets for surface coating [21].

Abrasive sheets	
Commercial name (grain)	**Absolute roughness ε**
P1000	$0{,}018\ mm$
P320	$0{,}046\ mm$
P120	$0{,}125\ mm$
P80	$0{,}210\ mm$
P40	$0{,}425\ mm$

.

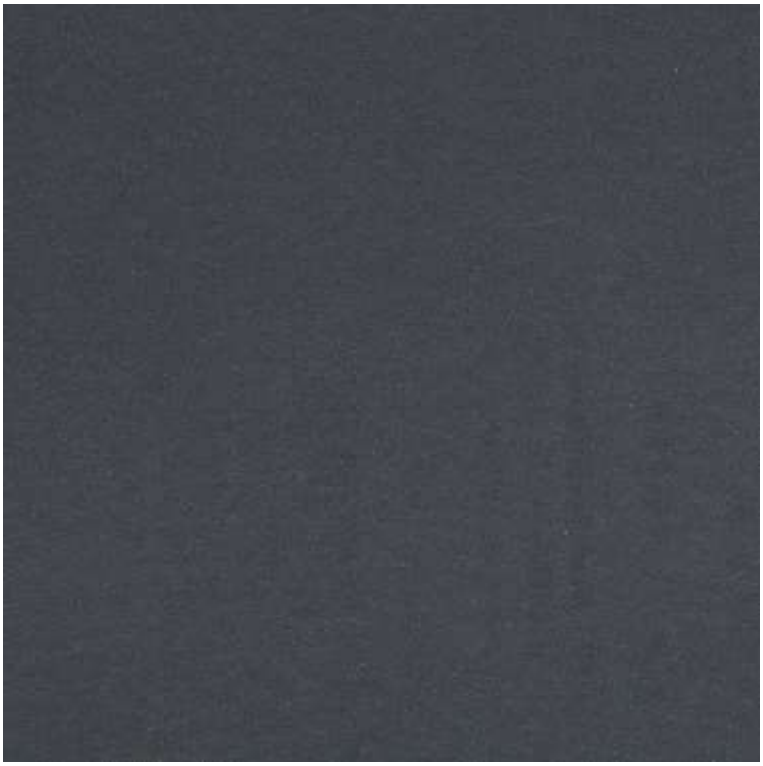

Figure 24. Abrasive sheet granulation P1000.

Figure 25. Abrasive sheet granulation P320.

Figure 26. Abrasive sheet granulation P120.

Figure 27. Abrasive sheet granulation P80.

Figure 28. Abrasive sheet granulation P40.

3.2 Characterization of the experimental set-up

The experimental apparatus of this work consists of an open circuit subsonic wind tunnel and the other components of the propulsion and measurement systems. The entire apparatus is available at the Fluid Mechanics and Hydraulics laboratory of the School of Technology and Management – Polytechnic Institute of Bragança – Portugal.

The wind tunnel provided is marketed by the company Armifield *Armifield* [22], which recommends its application in student learning and research activities, specially developed for simplified flow conditions and under low working speeds. A figure 29, shows the support bench of the tunnel with the components: axial suction fan, frequency inverter and a system of scales with weights and two graduated arms.

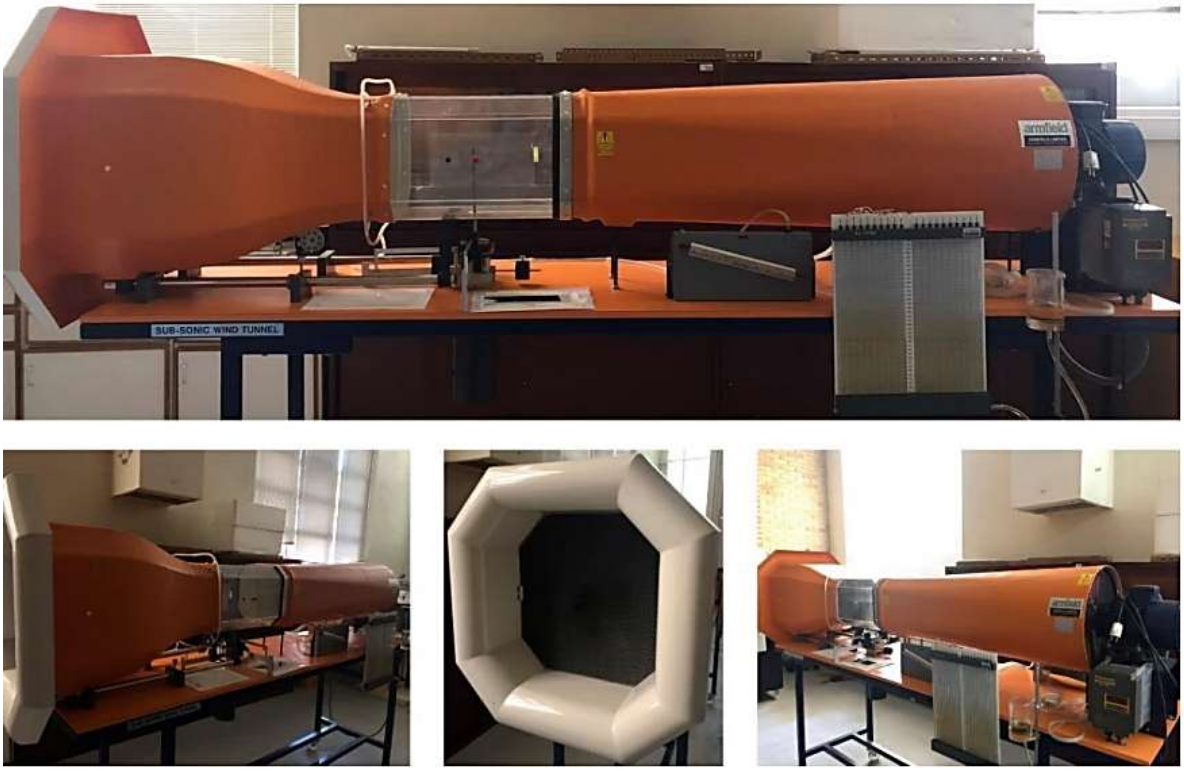

Figure 29. Open circuit subsonic Wind tunnel provided by IPB [23].

Figure 30. Drive and propulsion system [24].

The figure 30 shows the drive components at the output of the wind tunnel diffuser. The installation consists of a coupling between the fan and the shaft of an electric motor controlled by a frequency inverter Panasonic Inverter DV- 700. In this sense, the figure 31 presents a linear

adjustment of the shaft rotation associated with a flow velocity depending on the atmospheric conditions of the laboratory, in this case, at a pressure of 1 atmosphere and a temperature of 20 degrees Celsius. The electric motor works on the technical specifications presented in table 3.

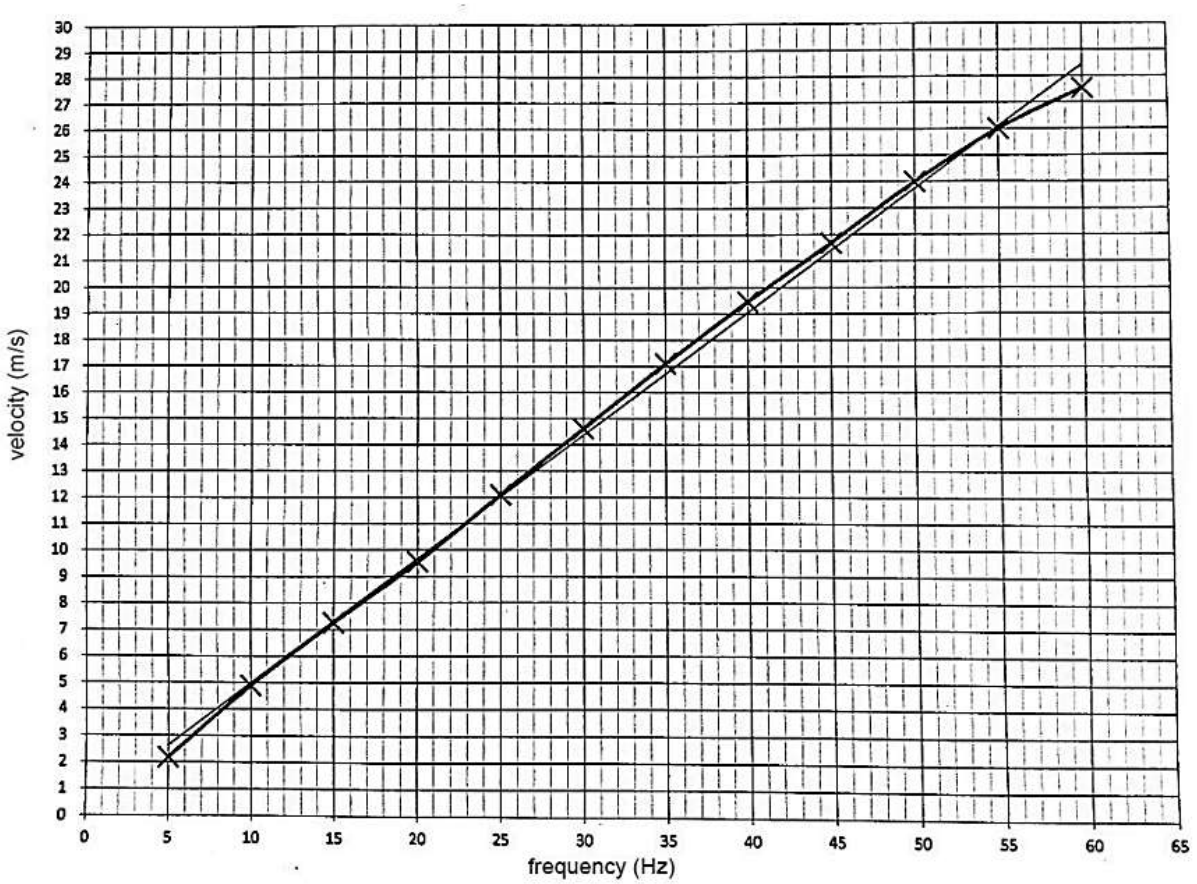

Figure 31. Relation of motor frequencies and airflow speeds.

Table 3. Electric motor technical specifications [23].

Technical specification	
Frequency	$60\ Hz$
Power	$1.5\ kW$
Voltage	$(220 - 240\ \Delta/380 - 415\ Y)$ V
Amperage	$(5{,}5 - 5{,}9\ \Delta/3{,}2\ \ - 3{,}4\ Y)A$
Rotation	$2850\ rpm$

According to figure 32, the location of the test section is observed: transparent, square geometry and made of acrylic, helping to visualize the flow. The catalogue of *Armifield* informs that the said square section is 30 centimeters high, 30 centimeters wide and 40 centimeters long, and can be easily retracted to facilitate the correct positioning of the bodies during the experiment.

From the figures it is also noted that inside the section, there is a vertical element attached to the measurement system that allows the body to be studied to be fixed. The measuring system consists of two scales and graduated rulers whose resolution is 0,01 newton. These rulers are perpendicular and simultaneously orthogonal to the vertical fastening element, all in turn, interconnected to the damping vessel.

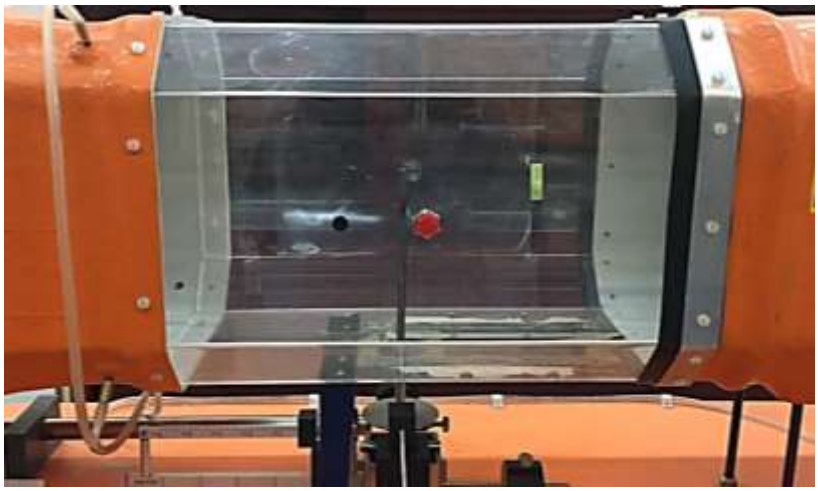

Figure 32-a. Subsonic wind tunnel test section *Armifield*.

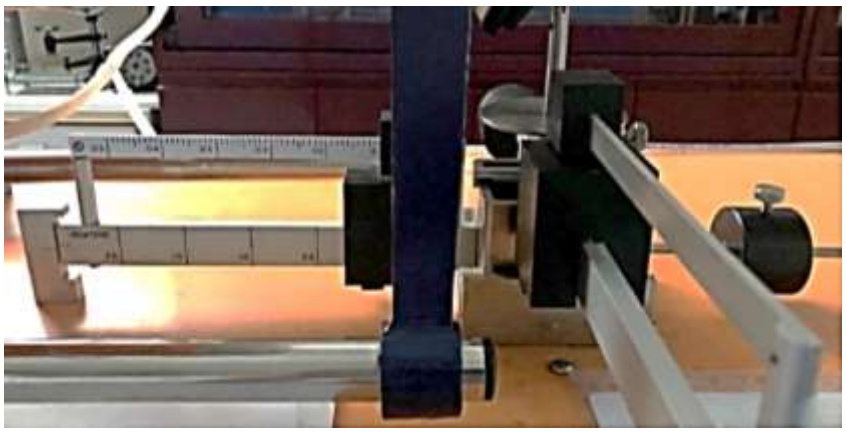

Figure 32-b. System of scales and graduated rulers.

3.3 Experimental procedure

The first consideration in the experimental methodology is to define the input parameters and conditions, that is, to characterize the flow. Thus, the definition of the flow regimes starts from the selection of the maximum operating speed, which allows to obtain the Reynolds number.

The figure 31 shows the test section in turn limited to a maximum speed of approximately 28 m/s, which is still sufficiently capable of transmitting disturbances through vibrations in the measuring system. Therefore, the velocity values were arbitrated aiming at the extension of the Reynolds number and taking into account the characteristic measure of the cylinders, the diameters. To simulate the transversal flows, the maximum velocity of this work was set at 20 m/s, which allows obtaining 17 points of study.

Table 4. Flow configuration.

Configuration	**Cylinder**		
	$\boldsymbol{i_1}$	$\boldsymbol{i_2}$	$\boldsymbol{i_3}$
Relationship L/D	3,75	2,50	1,25
Front area $A = LD$	$0{,}006\ m^2$	$0{,}004\ m^2$	$0{,}002\ m^2$
Velocity range V	$4\ m/s \leq V \leq 20\ m/s$		
Reynolds number Re	$1{,}1\ x\ 10^4 \leq Re \leq 5{,}3\ x\ 10^4$		

As for the effects of compressibility, since it is airflow, in this study its effects can be considered negligible, since under maximum speed conditions the Mach number has an approximately null value. For incompressible flow, the table 5, presents the properties of air during the experiments. Thus, in each cylinder i_n determined the properties of the fluid in standard atmospheric conditions, and the speed range, it was possible to know the flow regimes using the formulation of the Reynolds number.

Table 5. Air properties under incompressible flow conditions [2].

Environmental conditions ($\boldsymbol{Ma \approx 0}$)	
Pressure p	$1\ atm$
Temperature T	$20^0 C$
Density ρ	$1{,}20\ kg/m^3$
Dynamic viscosity μ	$1{,}80\ x\ 10^{-5}$

The characteristic measurement of the cylinders, the diameters D, and their lenghts L were also arbitrated in relation to the size of the test section so that the boundary layer on their surfaces would not be influenced by the proximity to the walls, which would certainly compromise the results. Next, each cylinder i_n fwas rigidly fixed to the measurement system and positioned in the center of the section so that it could be simulated in the order proposed figure 33.

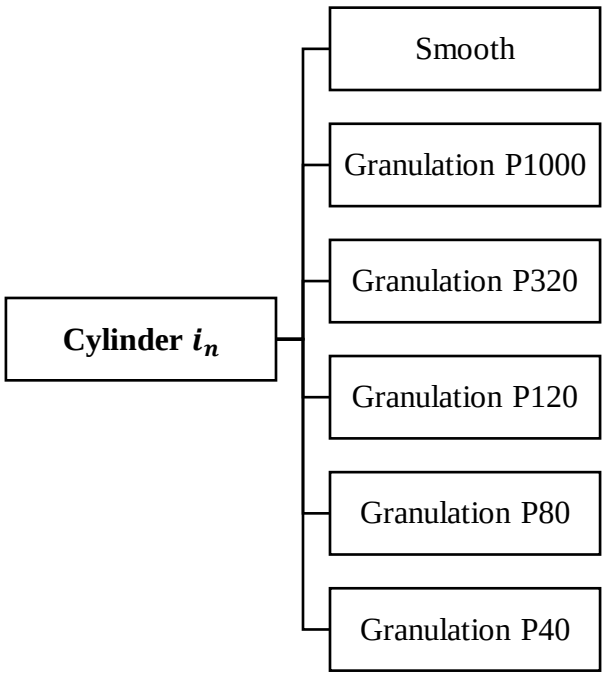

Figure 33. Sequence of experiments when selecting the cylinder i_n.

Figures 34 and 35 show the positioning of each cylinder to be studied. After this step, the test section was properly isolated with the aid of the sealing plate located in the lower hole of the test region. The complete isolation of this region allows for greater control of flow disturbances.

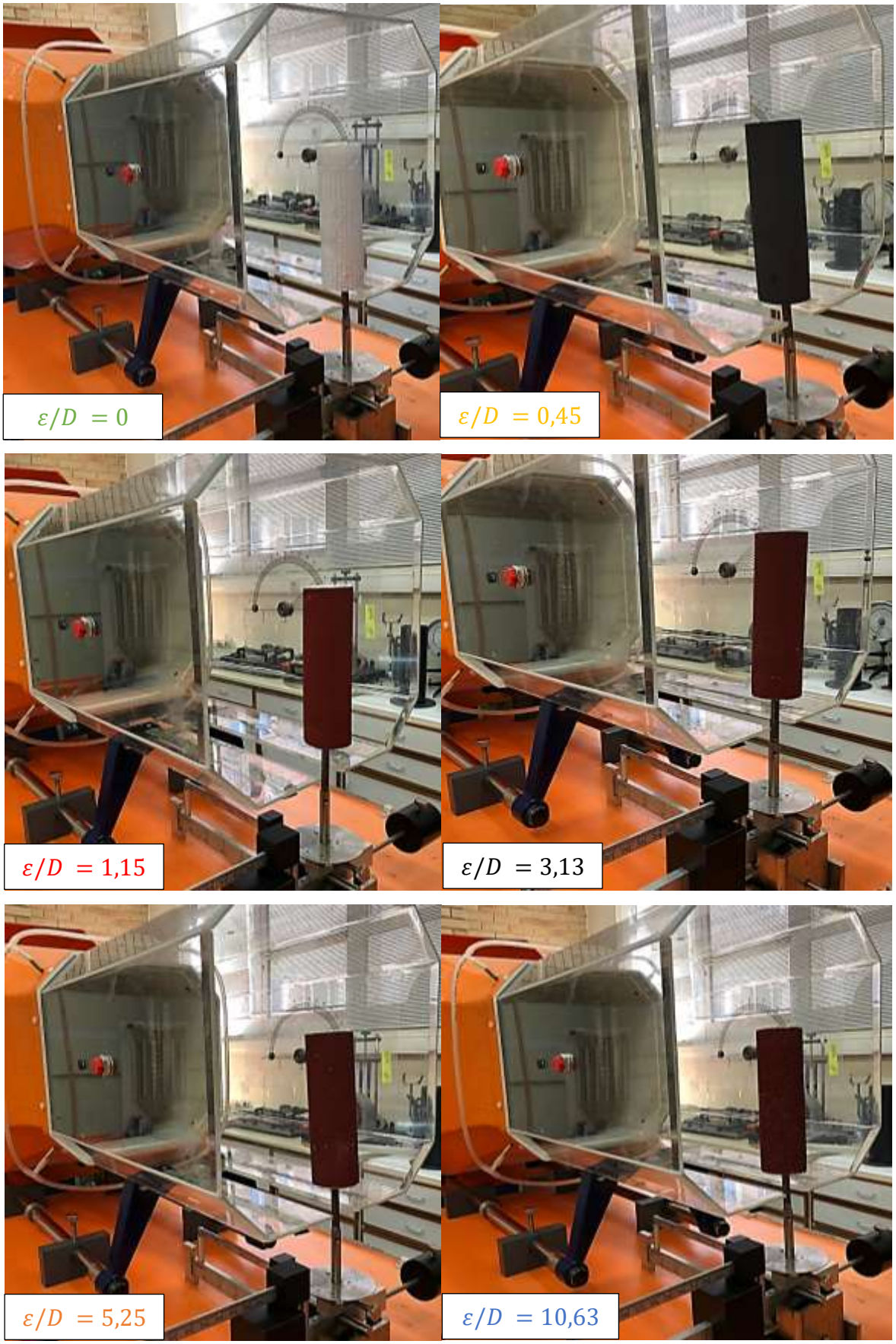

Figure 34. Simulation for the cylinder $\boldsymbol{i_1}$ with different relative roughness ε/D.

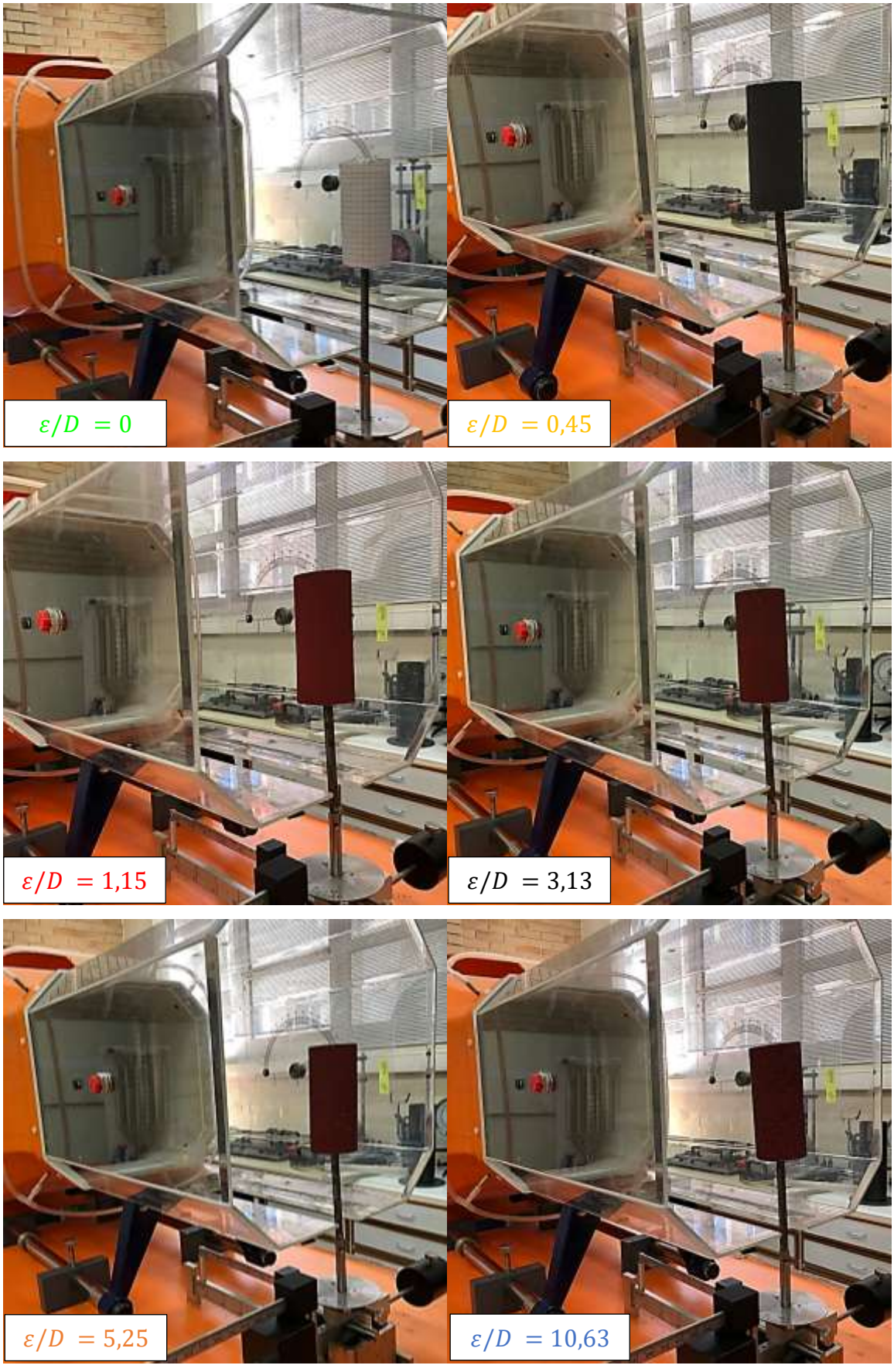

Figure 35. Simulation for the cylinder $\boldsymbol{i_2}$with different relative roughness ε/D.

Immediately before starting each of the simulations, the measuring system ruler was duly calibrated according to the position shown in figure 36. Through this system, the reading of the drag forces which are obtained by the sliding of the masses along the graduated ruler until equilibrium state is reached, that is, zero deflection.

Figure 36. Calibration of the measurement system.

Even though, given the aforementioned precautions, obtaining drag forces from the rough cylinders$i_3$was impossible because the aforementioned cylinder, when reached by the highest speed (fence of $20\ m/s$), it was accidentally dragged towards the fan's propeller causing it to rupture. Therefore, the project of a new propeller was requested, which so far, is under construction and has not yet been installed.

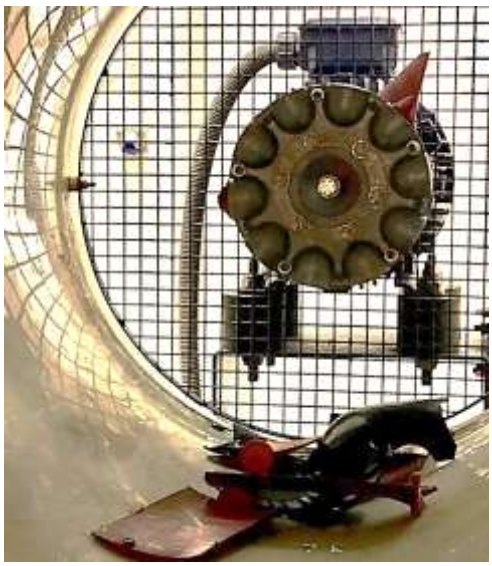

Figure 37-a. Accidental breakage of fan propeller.

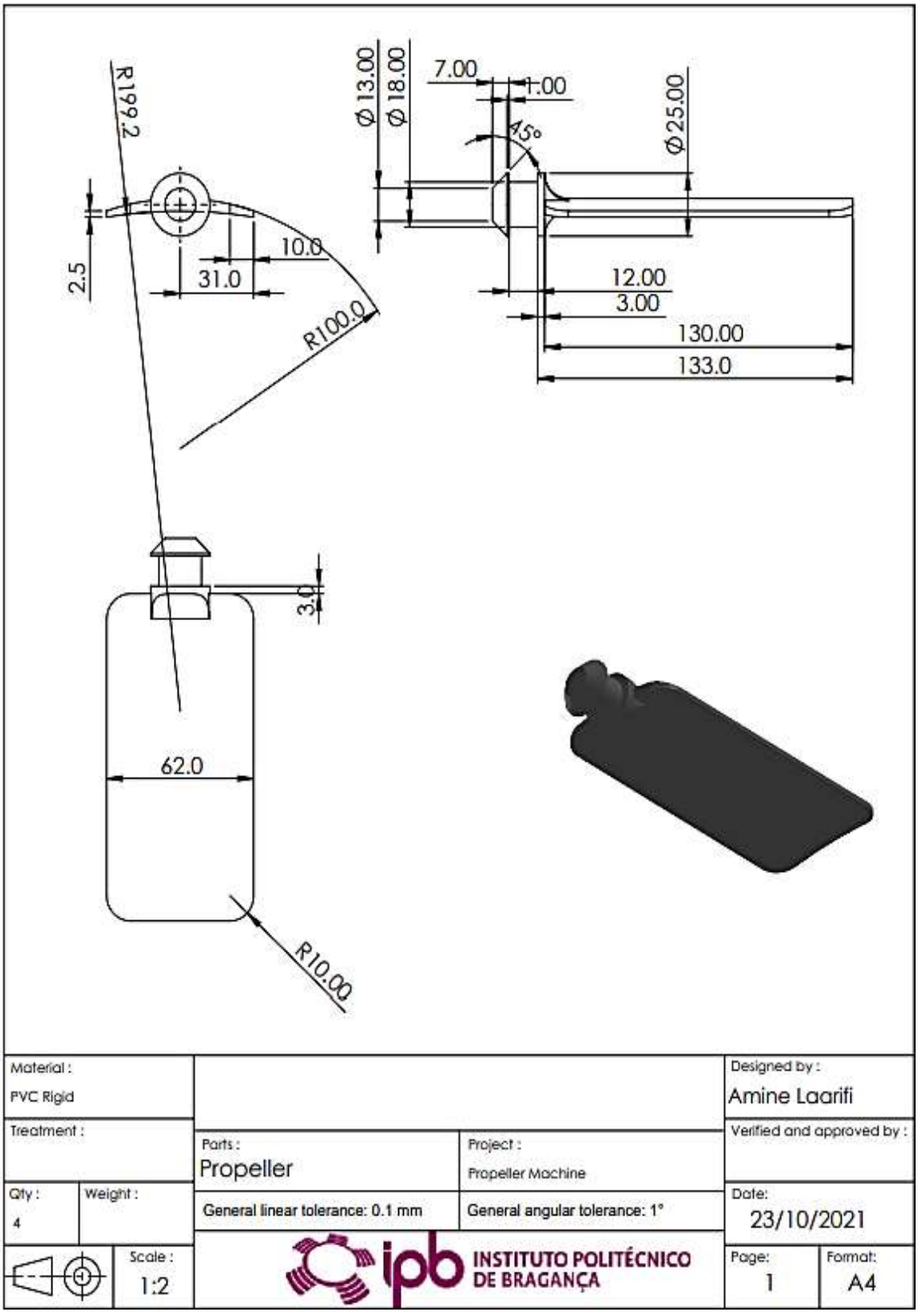

Figure 37-b. Propeller design for wind tunnel fan.

Chapter 4

Results and Discussions

In this chapter, the presentation and analysis of experimental data will be made. With these values it is possible to define the associated error in relation to the expected theoretical values and then, to carry out justified speculation about the observed behavior taking into account the presence of the surface roughness that were inserted.

4.1 Experimentation on smooth cylinders

Experimental validation consists of presenting the drag forces obtained, calculating the respective coefficients, and finally checking the errors by comparing the theoretical values taken as reference using the smooth cylinders $\boldsymbol{i_1}$, $\boldsymbol{i_2}$ e $\boldsymbol{i_3}$.

Rather, the preliminary force results are simultaneously compared against the expected drag $F_D$at each flow velocity ($V = V_\infty$) as outlined in chapter 2. Generally, it isknown that to determine the drag force, equation 35.

$$F_D = \frac{1}{2} C_D \, \rho A V^2 \tag{35}$$

Initially, to use the above equation and obtain the theoretical (expected) drag, it is necessary to perform linear interpolation of the coefficients expected (or theoretical) displayed in the figure 23, as it presents values adequate to the conditions of the study: laminar and external flow in smooth cylinders, as shown table 6. The expected drag force for each cylinder are presented in tables 7, 8 and 9.

Table 6. Expected drag coefficient for smooth cylinder (Theoretical).

Information	**Smooth Cylinder -** $(\varepsilon/D = 0)$		
	$\boldsymbol{i_1}$	$\boldsymbol{i_2}$	$\boldsymbol{i_3}$
Relationship L/D	3,75	2,50	1,25
Front Area $A = LD$	$0{,}006\ m^2$	$0{,}004\ m^2$	$0{,}002\ m^2$
Drag Coefficient $C_{D;expected}$ [2]	$\mathbf{0,76}$	$\mathbf{0,72}$	$\mathbf{0,63}$
Velocity Range V	$4\ m/s \leq V \leq 20\ m/s$		
Reynolds Number Re	$1{,}1\ x\ 10^4 \leq Re \leq 5{,}3\ x\ 10^4$		

Table 7. Comparison of drag force in the cylinder study $\boldsymbol{i_1}$.

Velocity $V\ (m/s)$	**Drag** $F_D\ (N)$		**Difference** %
	$F_{D;expected}$	$F_{D;experimental}$	
4	0,04	0,04	0
5	0,07	0,06	−14
6	0,10	0,08	−20
7	0,13	0,12	−8
8	0,18	0,15	−17
9	0,22	0,19	−14
10	0,27	0,24	−11
11	0,33	0,29	−12
12	0,39	0,30	−23
13	0,46	0,35	−24
14	0,54	0,44	−19
15	0,62	0,49	−21
16	0,70	0,59	−16
17	0,79	0,67	−15
18	0,89	0,76	−15
19	0,99	0,88	−11
20	1,09	0,98	−10

Table 8. Comparison of drag force in the cylinder study $\boldsymbol{i_2}$.

Velocity $V\ (m/s)$	**Drag** $F_D\ (N)$		**Difference** %
	$F_{D;expected}$	$F_{D;experimental}$	
4	0,03	0,02	−33
5	0,04	0,05	25
6	0,06	0,07	17
7	0,08	0,09	13
8	0,11	0,12	9
9	0,14	0,15	4
10	0,17	0,18	3
11	0,21	0,21	0
12	0,25	0,25	0
13	0,29	0,31	7
14	0,34	0,34	0
15	0,39	0,37	−5
16	0,44	0,48	9
17	0,50	0,55	10
18	0,56	0,63	13
19	0,62	0,73	18
20	0,69	0,90	30

Table 9. Comparison of drag force in the cylinder study $\boldsymbol{i_3}$.

Velocity $V\ (m/s)$	**Drag** $F_D\ (N)$		**Difference** %
	$F_{D;expected}$	$F_{D;experimental}$	
4	0,01	0,00	−100
5	0,02	0,00	−100
6	0,03	0,02	−27
7	0,04	0,04	8
8	0,05	0,06	24
9	0,06	0,07	14
10	0,08	0,08	6

11	0,09	0,10	9
12	0,11	0,15	38
13	0,13	0,19	49
14	0,15	0,23	55
15	0,17	0,27	59
16	0,19	0,30	55
17	0,22	0,33	51
18	0,24	0,35	43
19	(Unable to obtain)		
20			

In possession of the drag forces obtained experimentally for the cylinders $i_1, i_2, and\ i_3$, follow, according to the tables 10, 11 and 12, the calculation of their respective experimental coefficients, in turn compared to the expected coefficients (table 6), and determined by the equation 11.

It is noteworthy that the percentage determined is the expression of the difference between the values assumed to be true, that is, those expected or actual ($F_{D;expected}$ and $C_{D;expected}$) and those taken from the experimental results ($F_{D;experimental}$ and $C_{D;experimental}$). Thus, the mathematical expression for the relative error is given by equation 36, when calculating the relative error for drag forces, and equation 37 for their respective drag coefficients.

$$E_r(\%) = \frac{F_{D;experimental} - F_{D;expected}}{F_{D;expected}}\ x\ 100 \tag{36}$$

$$E_r(\%) = \frac{C_{D;experimental} - C_{D;expected}}{C_{D;expected}}\ x\ 100 \tag{37}$$

Table 10. Comparison between drag coefficients in the cylinder study $\boldsymbol{i_1}$.

Velocity $V\ (m/s)$	**Reynolds Number** Re	**Drag** $F_D\ (N)$ $F_{D;experimental}$	**Drag Coefficient** C_D		**Difference** %
			$C_{D;expected}$	$C_{D;experimental}$	
4	$1{,}1\ x10^4$	0,04	0,76	0,69	−8
5	$1{,}3\ x\ 10^4$	0,06		0,67	−12
6	$1{,}6\ x\ 10^4$	0,08		0,62	−19
7	$1{,}9\ x\ 10^4$	0,12		0,68	−10
8	$2{,}1\ x\ 10^4$	0,15		0,65	−14
9	$2{,}4\ x\ 10^4$	0,19		0,65	−14
10	$2{,}7\ x\ 10^4$	0,24		0,67	−12
11	$2{,}9\ x\ 10^4$	0,29		0,67	−12
12	$3{,}2\ x\ 10^4$	0,30		0,58	−24
13	$3{,}5\ x\ 10^4$	0,35		0,58	−24
14	$3{,}7\ x\ 10^4$	0,44		0,62	−18
15	$4{,}0\ x\ 10^4$	0,49		0,60	−20
16	$4{,}3\ x\ 10^4$	0,59		0,64	−16
17	$4{,}5\ x\ 10^4$	0,67		0,64	−15
18	$4{,}8\ x\ 10^4$	0,76		0,65	−14
19	$5{,}1\ x\ 10^4$	0,88		0,68	−11
20	$5{,}3\ x\ 10^4$	0,98		0,68	−10

Table 11. Comparison between drag coefficients in the cylinder study $\boldsymbol{i_2}$.

Velocity $V\ (m/s)$	**Reynolds Number** Re	**Drag** $F_D\ (N)$ $F_{D;experimental}$	**Drag Coefficient** C_D		**Difference** %
			$C_{D;expected}$	$C_{D;experimental}$	
4	$1{,}1\ x10^4$	0,02	0,72	0,52	−28
5	$1{,}3\ x\ 10^4$	0,05		0,83	16
6	$1{,}6\ x\ 10^4$	0,07		0,81	13
7	$1{,}9\ x\ 10^4$	0,09		0,77	6

8	$2{,}1\ x\ 10^4$	0,12		0,78	9
9	$2{,}4\ x\ 10^4$	0,15		0,75	4
10	$2{,}7\ x\ 10^4$	0,18		0,73	1
11	$2{,}9\ x\ 10^4$	0,21		0,72	0
12	$3{,}2\ x\ 10^4$	0,25		0,72	0
13	$3{,}5\ x\ 10^4$	0,31		0,76	6
14	$3{,}7\ x\ 10^4$	0,34		0,72	0
15	$4{,}0\ x\ 10^4$	0,37		0,69	−5
16	$4{,}3\ x\ 10^4$	0,48		0,78	9
17	$4{,}5\ x\ 10^4$	0,55		0,79	10
18	$4{,}8\ x\ 10^4$	0,63		0,81	13
19	$5{,}1\ x\ 10^4$	0,73		0,84	17
20	$5{,}3\ x\ 10^4$	0,90		0,94	30

Table 12. Comparison between drag coefficients in the cylinder study $\boldsymbol{i_3}$.

Velocity $V\ (m/s)$	**Reynolds Number** Re	**Drag** $F_D\ (N)$ $F_{D;experimental}$	**Drag Coefficient** C_D		**Difference** %
			$C_{D;expected}$	$C_{D;experimental}$	
4	$1{,}1\ x10^4$	0,00	0,63	0,00	−100
5	$1{,}3\ x\ 10^4$	0,00		0,00	−100
6	$1{,}6\ x\ 10^4$	0,02		0,46	−27
7	$1{,}9\ x\ 10^4$	0,04		0,68	8
8	$2{,}1\ x\ 10^4$	0,06		0,78	24
9	$2{,}4\ x\ 10^4$	0,07		0,72	14
10	$2{,}7\ x\ 10^4$	0,08		0,67	6
11	$2{,}9\ x\ 10^4$	0,10		0,69	9
12	$3{,}2\ x\ 10^4$	0,15		0,87	38
13	$3{,}5\ x\ 10^4$	0,19		0,94	49
14	$3{,}7\ x\ 10^4$	0,23		0,98	55
15	$4{,}0\ x\ 10^4$	0,27		1,00	59
16	$4{,}3\ x\ 10^4$	0,30		0,98	55

17	$4{,}5\ x\ 10^4$	0,33		0,95	051
18	$4{,}8\ x\ 10^4$	0,35		0,90	43
19	(Unable to obtain)				
20					

4.2 Insertion of surface roughness

At this moment, the force results are presented to obtain the drag coefficients for the cylinders $\boldsymbol{i_1}$ and $\boldsymbol{i_2}$ under the effect of the inserted roughness, which must be done by adding another analysis variable, the relative roughness $\frac{\varepsilon}{D}$. Thus, the drag coefficients are analyzed according to the condition below, starting from the comparison between values of drag force.

$$C_D = f(Re, \frac{\varepsilon}{D}) \tag{38}$$

Table 13. Drag forces in the cylinder study $\boldsymbol{i_1}$ under different roughness.

Velocity $V\ (m/s)$	**Drag** - $F_{D;experimental}\ (N)$					
	$\frac{\varepsilon}{D} = 0$	$\frac{\varepsilon}{D} = 0{,}45$	$\frac{\varepsilon}{D} = 1{,}15$	$\frac{\varepsilon}{D} = 3{,}13$	$\frac{\varepsilon}{D} = 5{,}25$	$\frac{\varepsilon}{D} = 10{,}63$
4	0,04	0,04	0,03	0,04	0,04	0,04
5	0,06	0,06	0,06	0,06	0,06	0,07
6	0,08	0,09	0,09	0,09	0,10	0,10
7	0,12	0,13	0,13	0,13	0,13	0,13
8	0,15	0,16	0,16	0,16	0,17	0,18
9	0,19	0,20	0,20	0,20	0,21	0,22
10	0,24	0,26	0,25	0,25	0,26	0,26
11	0,29	0,31	0,30	0,30	0,32	0,33
12	0,30	0,35	0,35	0,35	0,35	0,35

13	0,35	0,37	0,38	0,39	0,39	0,38
14	0,44	0,50	0,45	0,47	0,48	0,43
15	0,49	0,46	0,50	0,55	0,55	0,51
16	0,59	0,60	0,62	0,65	0,64	0,63
17	0,67	0,69	0,70	0,73	0,72	0,73
18	0,76	0,78	0,80	0,83	0,85	0,80
19	0,88	0,90	0,94	0,94	0,80	0,92
20	0,98	1,00	1,50	1,80	0,88	1,50

Table 14. Drag forces in the cylinder study $\boldsymbol{i_2}$ under different roughness.

Velocity $V\ (m/s)$	**Drag** - $F_{D;experimental}\ (N)$					
	$\frac{\varepsilon}{D} = 0$	$\frac{\varepsilon}{D} = 0{,}45$	$\frac{\varepsilon}{D} = 1{,}15$	$\frac{\varepsilon}{D} = 3{,}13$	$\frac{\varepsilon}{D} = 5{,}25$	$\frac{\varepsilon}{D} = 10{,}63$
4	0,02	0,02	0,02	0,02	0,02	0,02
5	0,05	0,05	0,05	0,05	0,05	0,06
6	0,07	0,08	0,08	0,08	0,08	0,09
7	0,09	0,10	0,10	0,10	0,10	0,10
8	0,12	0,13	0,13	0,13	0,14	0,14
9	0,15	0,15	0,15	0,15	0,16	0,17
10	0,18	0,19	0,18	0,18	0,19	0,19
11	0,21	0,22	0,22	0,22	0,23	0,24
12	0,25	0,29	0,29	0,29	0,29	0,29
13	0,31	0,33	0,34	0,35	0,35	0,34
14	0,34	0,39	0,35	0,36	0,37	0,33
15	0,37	0,35	0,38	0,42	0,42	0,39
16	0,48	0,49	0,50	0,53	0,52	0,51
17	0,55	0,57	0,57	0,60	0,59	0,60
18	0,63	0,65	0,66	0,69	0,70	0,66
19	0,73	0,75	0,78	0,78	0,66	0,76
20	0,90	0,92	1,38	1,65	0,81	1,38

Table 15. Drag coefficients in the cylinder study $\boldsymbol{i_1}$ under different roughness.

Reynolds Number Re	**Drag Coefficient** - $C_{D;experimental}\ (N)$					
	$\frac{\varepsilon}{D} = 0$	$\frac{\varepsilon}{D} = 0{,}45$	$\frac{\varepsilon}{D} = 1{,}15$	$\frac{\varepsilon}{D} = 3{,}13$	$\frac{\varepsilon}{D} = 5{,}25$	$\frac{\varepsilon}{D} = 10{,}63$
$1{,}1\ x10^4$	0,69	0,69	0,52	0,61	0,64	0,64
$1{,}3\ x\ 10^4$	0,67	0,67	0,67	0,67	0,67	0,78
$1{,}6\ x\ 10^4$	0,62	0,69	0,69	0,69	0,73	0,77
$1{,}9\ x\ 10^4$	0,68	0,74	0,74	0,74	0,74	0,74
$2{,}1\ x\ 10^4$	0,65	0,69	0,69	0,69	0,74	0,76
$2{,}4\ x\ 10^4$	0,65	0,69	0,67	0,69	0,72	0,75
$2{,}7\ x\ 10^4$	0,67	0,72	0,69	0,69	0,72	0,72
$2{,}9\ x\ 10^4$	0,67	0,71	0,69	0,69	0,73	0,76
$3{,}2\ x\ 10^4$	0,58	0,68	0,68	0,68	0,68	0,68
$3{,}5\ x\ 10^4$	0,58	0,61	0,62	0,64	0,64	0,62
$3{,}7\ x\ 10^4$	0,62	0,71	0,64	0,67	0,68	0,61
$4{,}0\ x\ 10^4$	0,60	0,57	0,62	0,68	0,68	0,63
$4{,}3\ x\ 10^4$	0,64	0,65	0,67	0,71	0,69	0,68
$4{,}5\ x\ 10^4$	0,64	0,66	0,67	0,70	0,69	0,70
$4{,}8\ x\ 10^4$	0,65	0,67	0,69	0,71	0,73	0,69
$5{,}1\ x\ 10^4$	0,68	0,69	0,72	0,72	0,62	0,71
$5{,}3\ x\ 10^4$	0,68	0,69	1,04	1,25	0,61	1,04

Table 16. Drag coefficients in the cylinder study $\boldsymbol{i_2}$ under different roughness.

Reynolds Number Re	**Drag Coefficient** - $C_{D;experimental}\ (N)$					
	$\frac{\varepsilon}{D} = 0$	$\frac{\varepsilon}{D} = 0{,}45$	$\frac{\varepsilon}{D} = 1{,}15$	$\frac{\varepsilon}{D} = 3{,}13$	$\frac{\varepsilon}{D} = 5{,}25$	$\frac{\varepsilon}{D} = 10{,}63$
$1{,}1\ x10^4$	0,52	0,52	0,39	0,46	0,48	0,48
$1{,}3\ x\ 10^4$	0,83	0,83	0,83	0,83	0,83	0,97
$1{,}6\ x\ 10^4$	0,81	0,91	0,91	0,91	0,96	1,01
$1{,}9\ x\ 10^4$	0,77	0,83	0,83	0,83	0,83	0,83

$2{,}1\ x\ 10^4$	0,78	0,83	0,83	0,83	0,89	0,91
$2{,}4\ x\ 10^4$	0,75	0,79	0,77	0,79	0,82	0,86
$2{,}7\ x\ 10^4$	0,73	0,79	0,76	0,76	0,79	0,79
$2{,}9\ x\ 10^4$	0,72	0,77	0,75	0,75	0,80	0,82
$3{,}2\ x\ 10^4$	0,72	0,84	0,84	0,84	0,84	0,84
$3{,}5\ x\ 10^4$	0,76	0,81	0,83	0,85	0,85	0,83
$3{,}7\ x\ 10^4$	0,72	0,82	0,74	0,77	0,79	0,71
$4{,}0\ x\ 10^4$	0,69	0,64	0,70	0,77	0,77	0,71
$4{,}3\ x\ 10^4$	0,78	0,79	0,82	0,86	0,85	0,83
$4{,}5\ x\ 10^4$	0,79	0,82	0,83	0,86	0,85	0,86
$4{,}8\ x\ 10^4$	0,81	0,83	0,85	0,88	0,91	0,85
$5{,}1\ x\ 10^4$	0,84	0,86	0,90	0,90	0,77	0,88
$5{,}3\ x\ 10^4$	0,94	0,96	1,43	1,72	0,84	1,43

4.3 Considerations about the results

The analysis of results takes place objectively through comparative graphs as they facilitate the visualization of behaviors as they also guide the discussions. The first considerations are related to the force data obtained (tables 7, 8 and 9), and the respective calculated drag coefficients (tables 10, 11 and 12) on smooth cylinders whose comparative graphics are in the figures 38 and 39.

Visualization of graphics of figures 40, 41 and 42 show significant variations in drag coefficient, especially for cylinders $\boldsymbol{i_1}$ and $\boldsymbol{i_3}$ since in these cylinders, there were more variations in forces as the flow velocity increased, with the main extrapolations in the last force value obtained, which may have been due to the difficulty in keeping the measurement system stable and without vibrations at high speeds.

The experimental results of the cylinder presented in $\boldsymbol{i_2}$ figure 41, proved to be more acceptable quantitatively, as along the study points showed smaller variations in drag forces in relation to the expected value. Despite this, the data obtained in the resolution of the measurement system used (0.01 newton) account for the significant divergences in its

respective drag coefficient, suggesting the need to provide a system that enables the force reading with more decimal places for a quantitative analysis more reliable in the calculation of drag coefficients. It is useful to mention that the smallest percentage differences for force and drag coefficients were concentrated even slightly before the central value of the speed range, which can be seen when viewing their respective tables and the graphic behavior in the figures 40, 41 and 42.

Although a constant value of drag coefficients was expected for the strip $1{,}1\ x\ 10^4 \leq Re \leq 5{,}3\ x\ 10^4$, the differences observed especially the cylinders $\boldsymbol{i_1}$ and $\boldsymbol{i_2}$ do not preclude an acceptable qualitative analysis for student purposes since the typical behavior in these bodies is predictably a constant straight line even before the crisis of the drag, which, given this knowledge, could be assumed when visualizing the fluctuation of the study points around a central value, although this fluctuation did not occur along the constant line relative to the expected (or theoretical) values, which it only occurred reasonably for the cylinder drag coefficients $\boldsymbol{i_2}$.

Through a qualitative analysis, the insertion of rough sand paper brought different behaviors for the drag coefficients which can be compared individually according to the different relative roughness $\frac{\varepsilon}{D}$ in the graphics of figures 44 and 46. In the force graphs (figures 43 and 45), there is a slight difference between values of drag forces for the same model with the insertion of roughness, which may have occurred due to variations in the friction portion and increase in turbulence in the laminar boundary layer through coarse sand paper grains.

In the observation of drag coefficients, as the relative roughness increased, the results show that the response to the insertion of roughness is an approximate expression of the behavior observed for the smooth model. In general in the range $1{,}1\ x\ 10^4 \leq Re \leq 5{,}3\ x\ 10^4$, the rough surfaces presented values of drag coefficients that were increasingly higher as the relative roughness increased, and there was clearly no sudden or sudden change in the coefficients as it was possible to have occurred since the phenomenon of the crisis of the drag occurs in lower Reynolds numbers in rougher models. However, it is difficult to suppose that this could have happened in this study, since, as the flow velocity increased, the influence of vibrations on the measurement system increased, which, as already mentioned, caused some instability in the results.

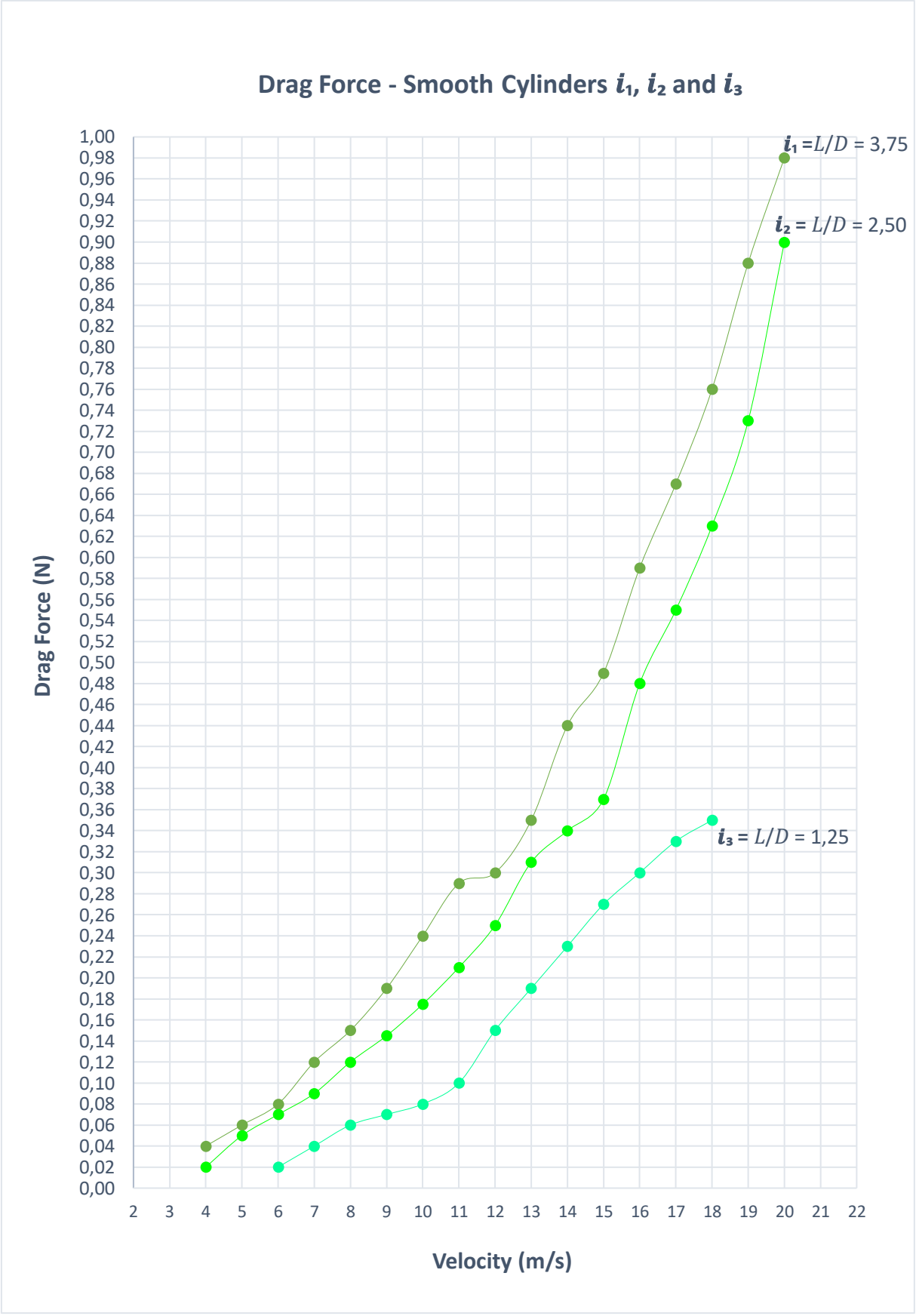

Figure 38. Behavior of drag forces obtained in different L/D.

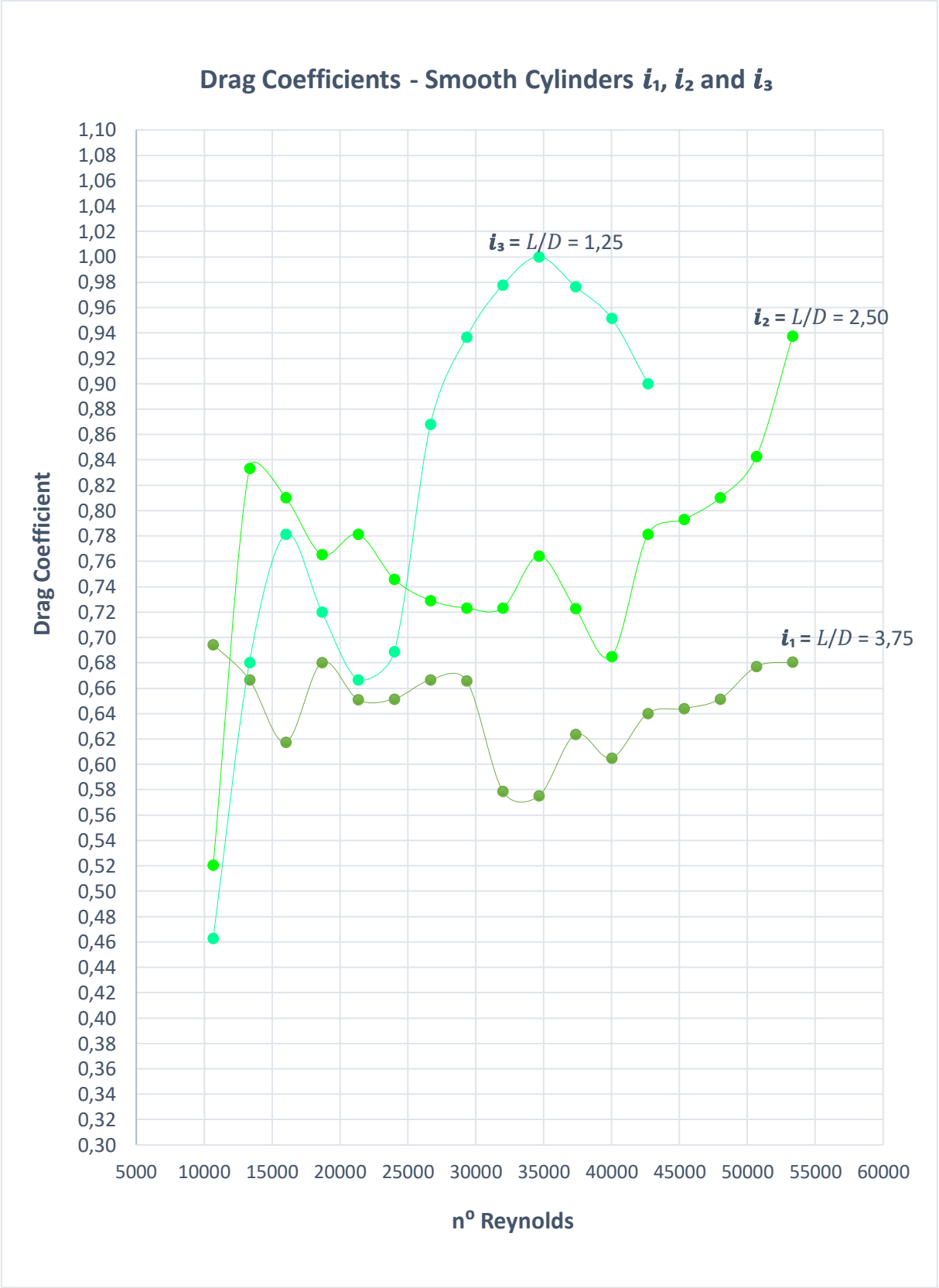

Figure 39. Behavior of drag coefficients obtained in different L/D.

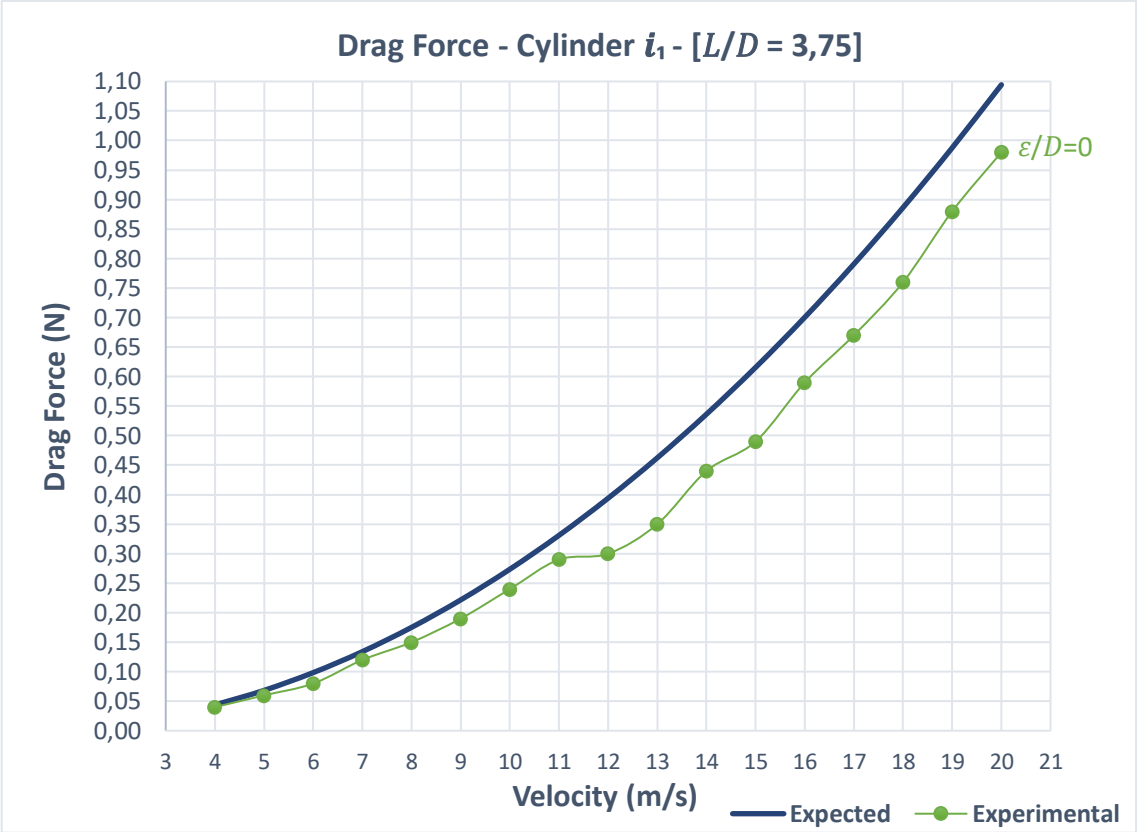

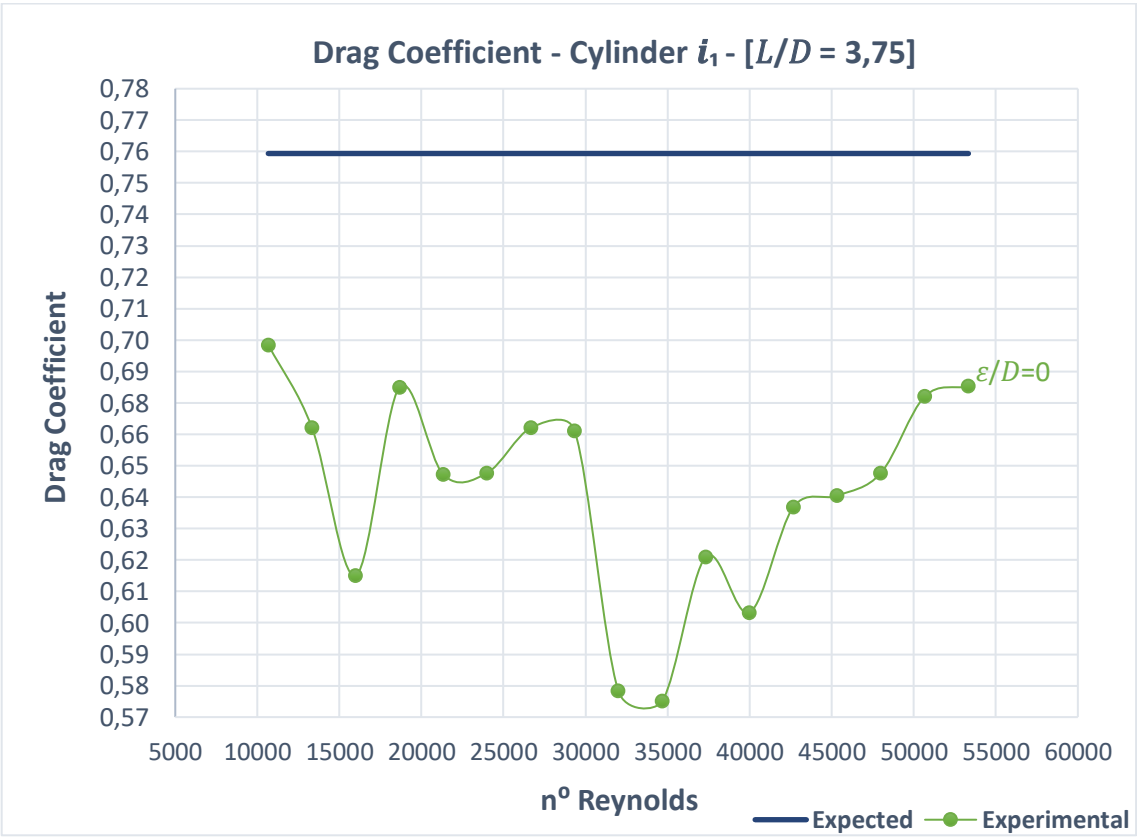

Figure 40. Expected and experimental results for cylinder i_1.

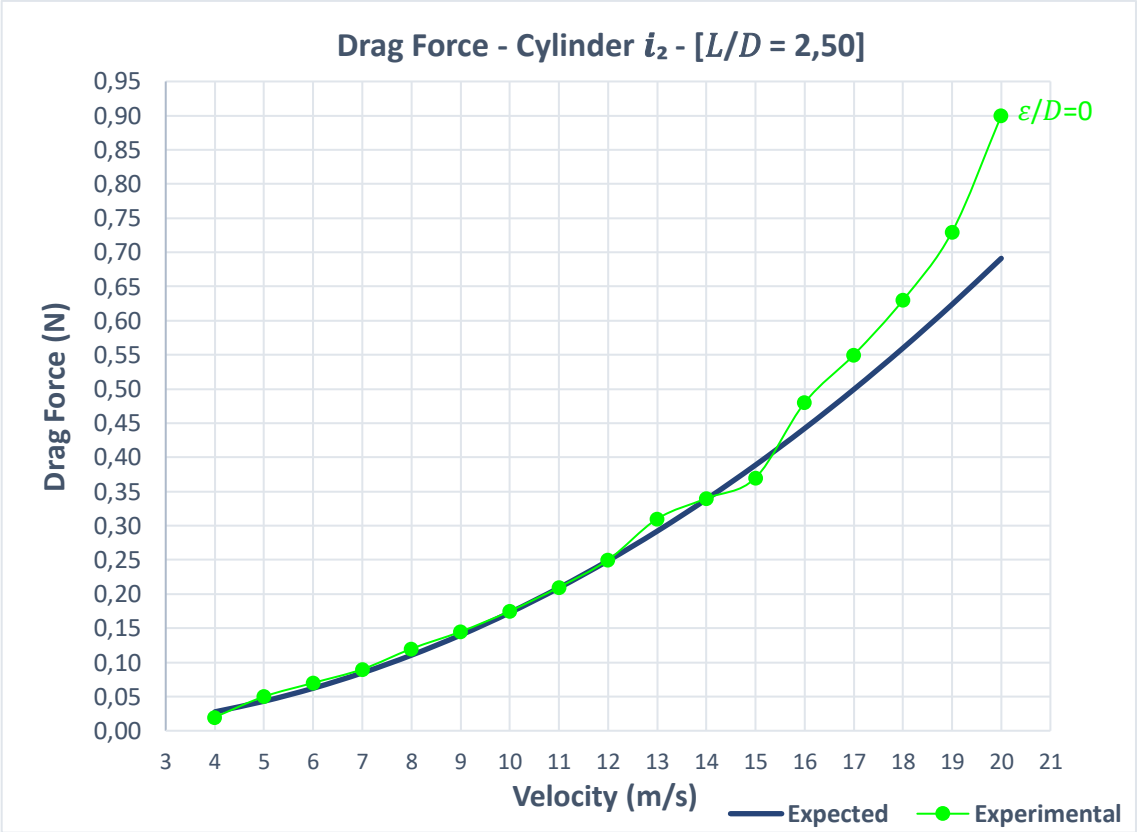

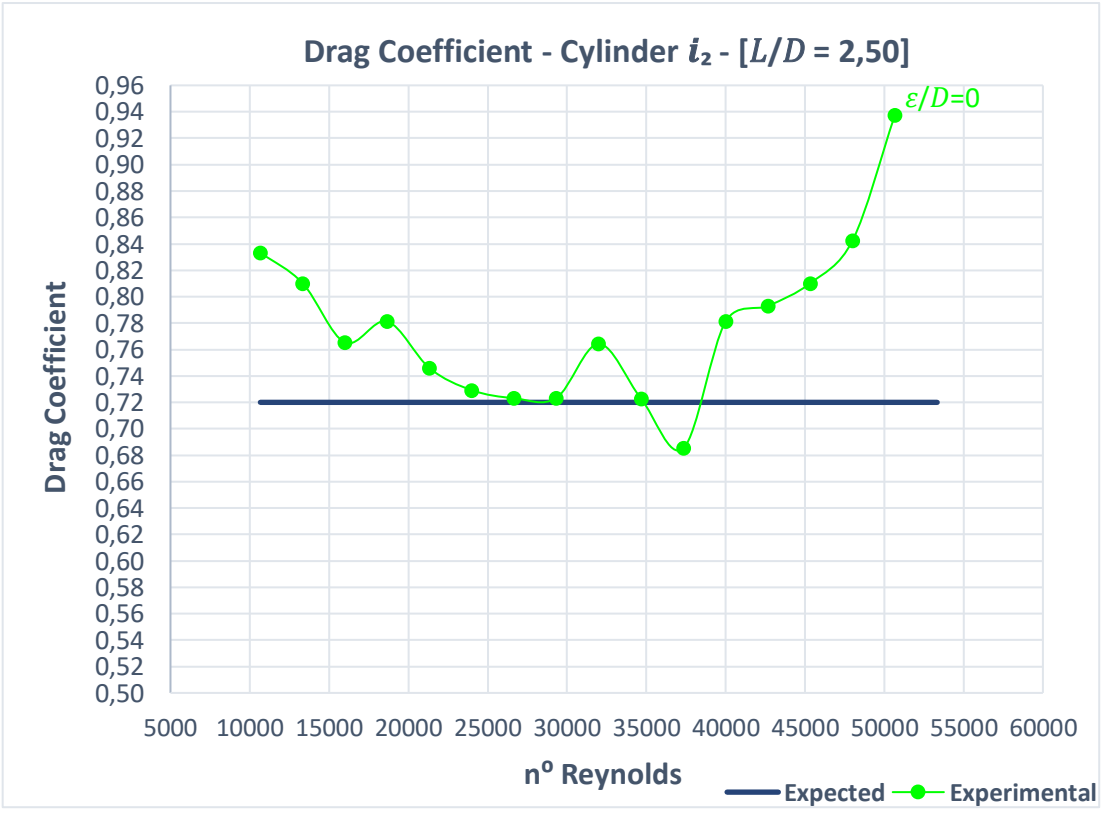

Figure 41. Expected and experimental results for cylinder i_2.

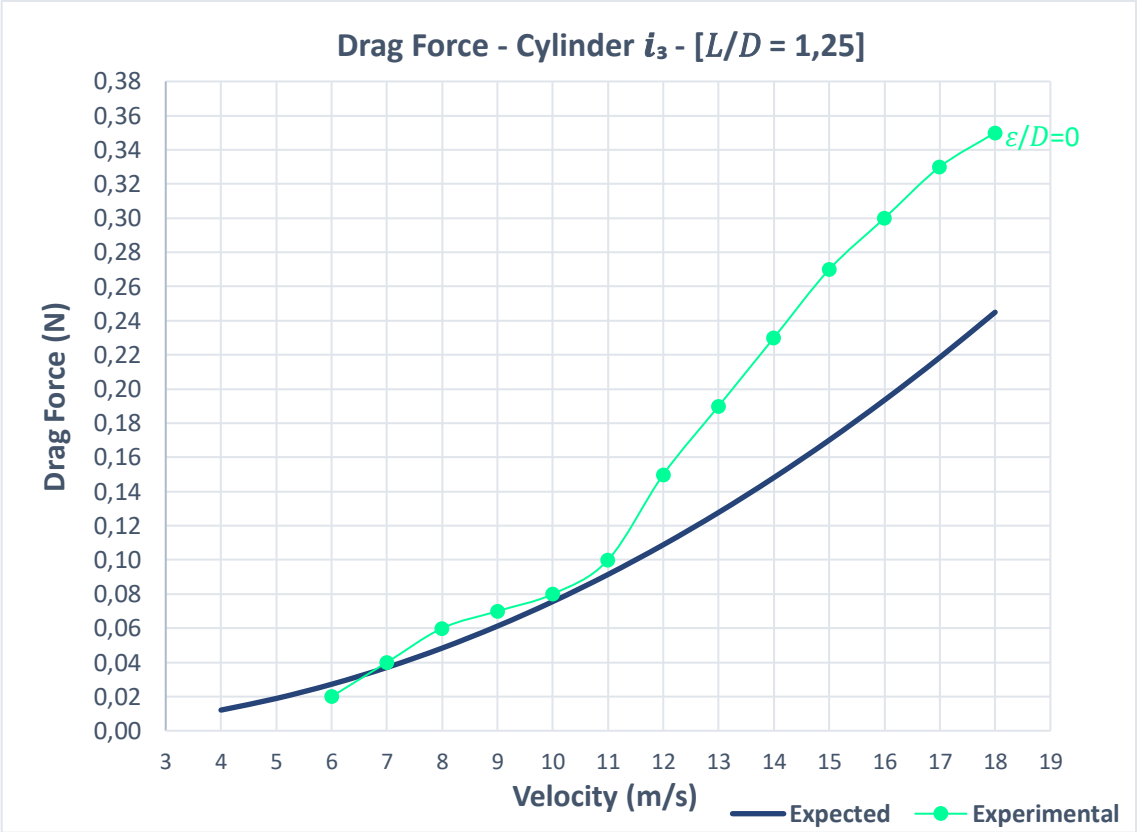

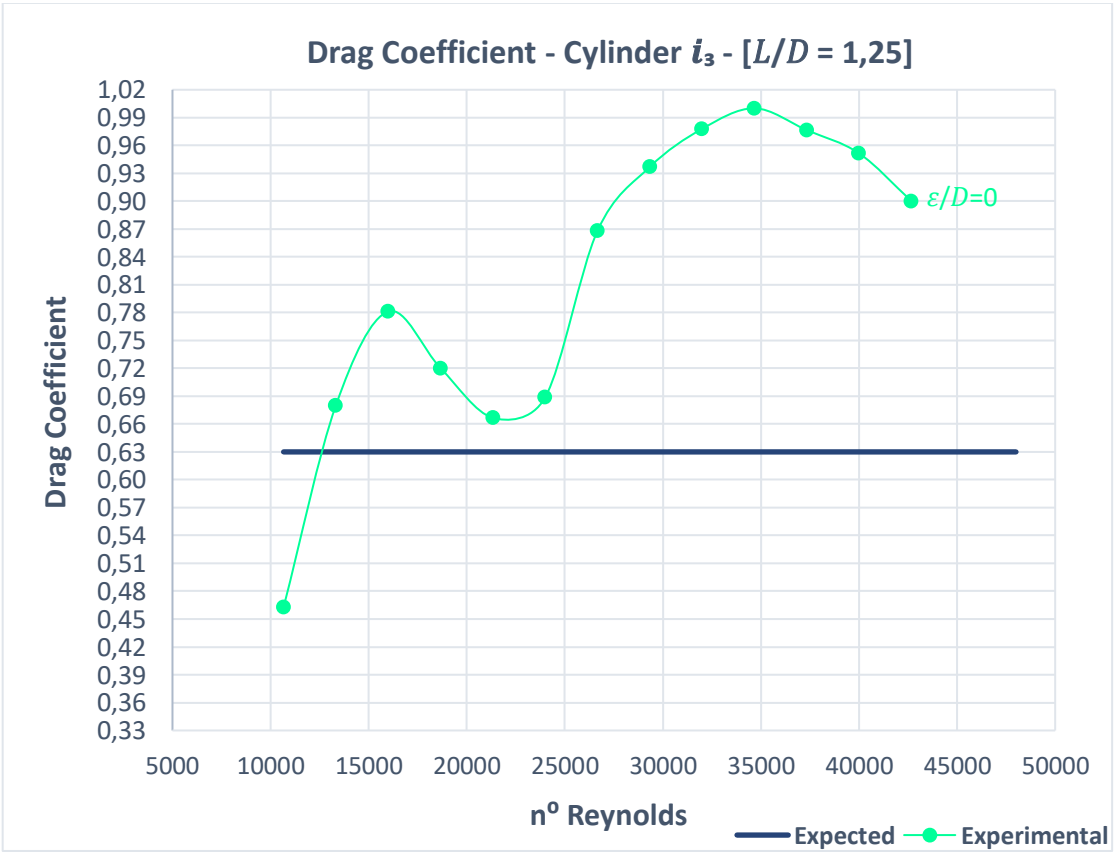

Figure 42. Expected and experimental results for cylinder i_3.

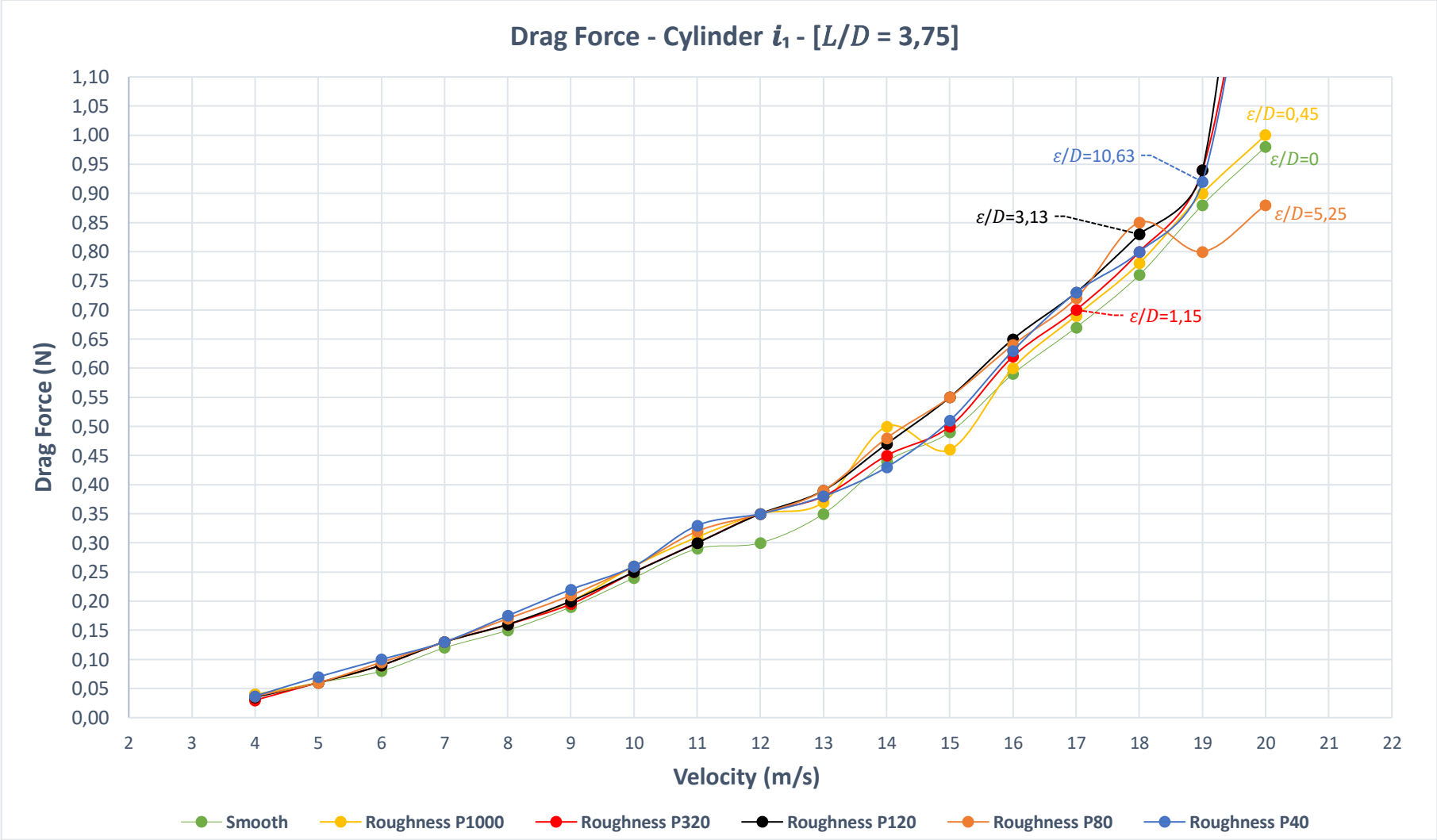

Figure 43. Comparative drag forces for cylinder i_1 considering the different relative roughness $\frac{\varepsilon}{D}$.

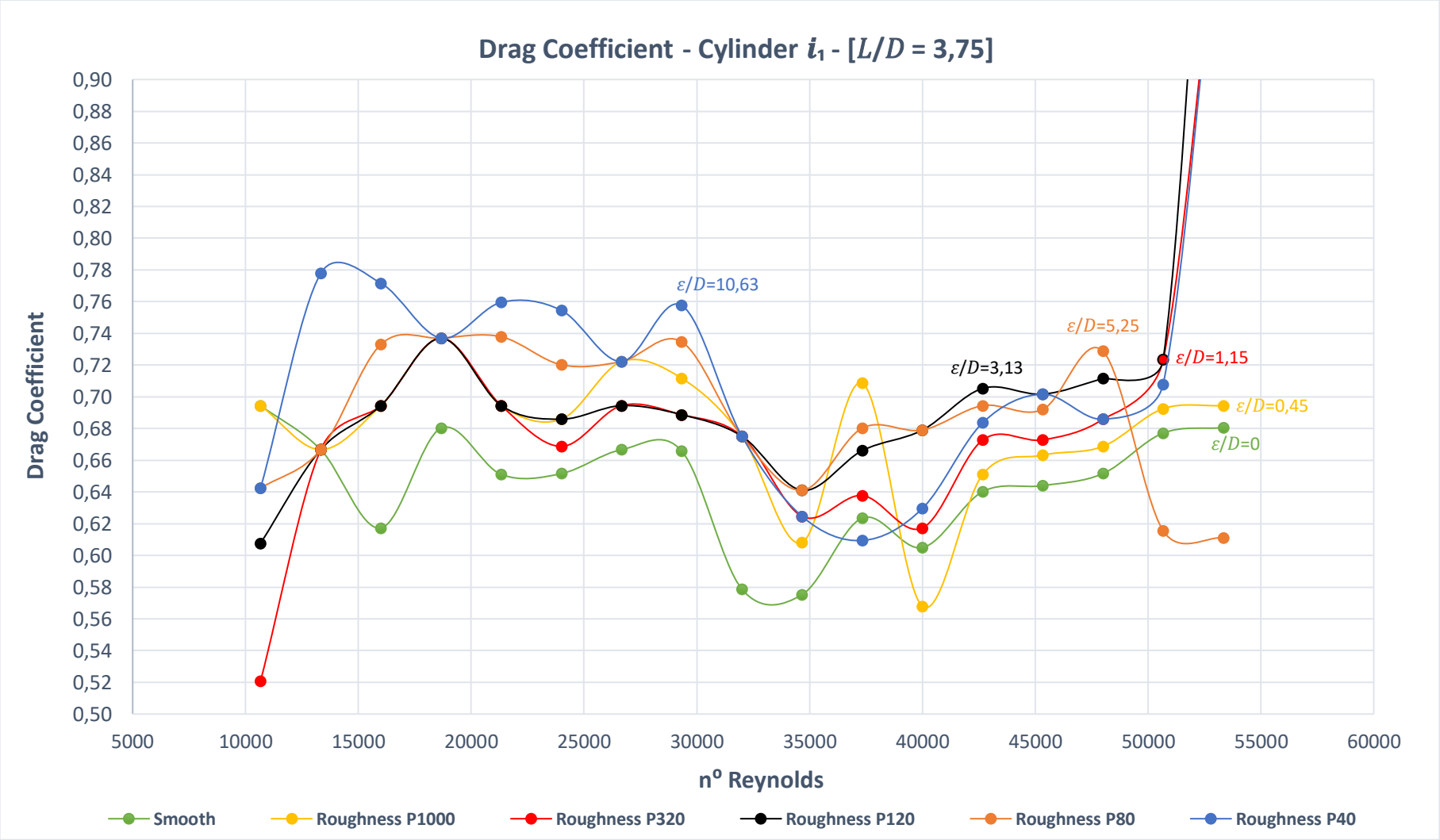

Figure 44. Comparative drag coefficients for cylinder i_1 considering the different relative roughness $\frac{\varepsilon}{D}$.

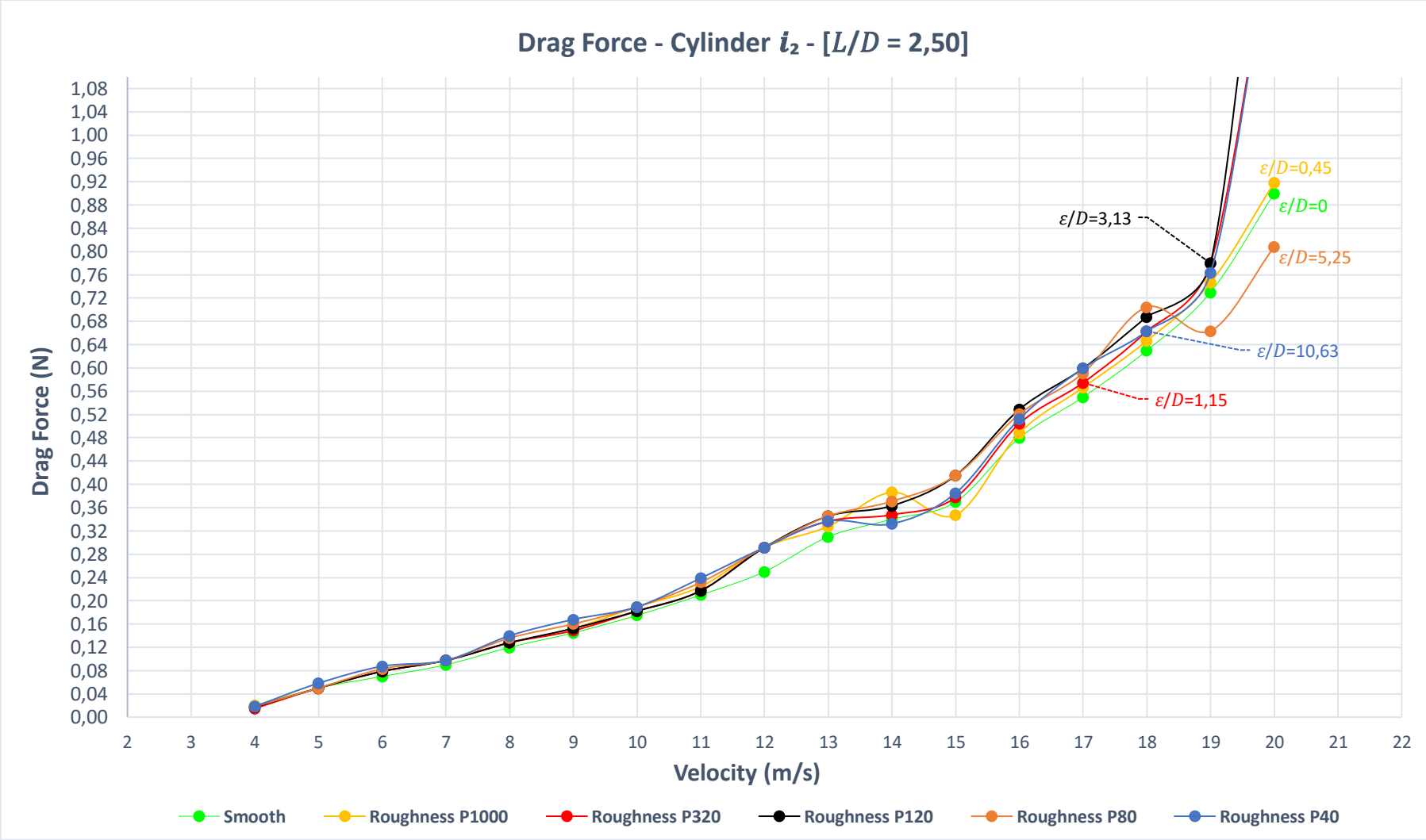

Figure 45. Comparative drag forces for cylinder i_2 considering the different relative roughness $\frac{\varepsilon}{D}$.

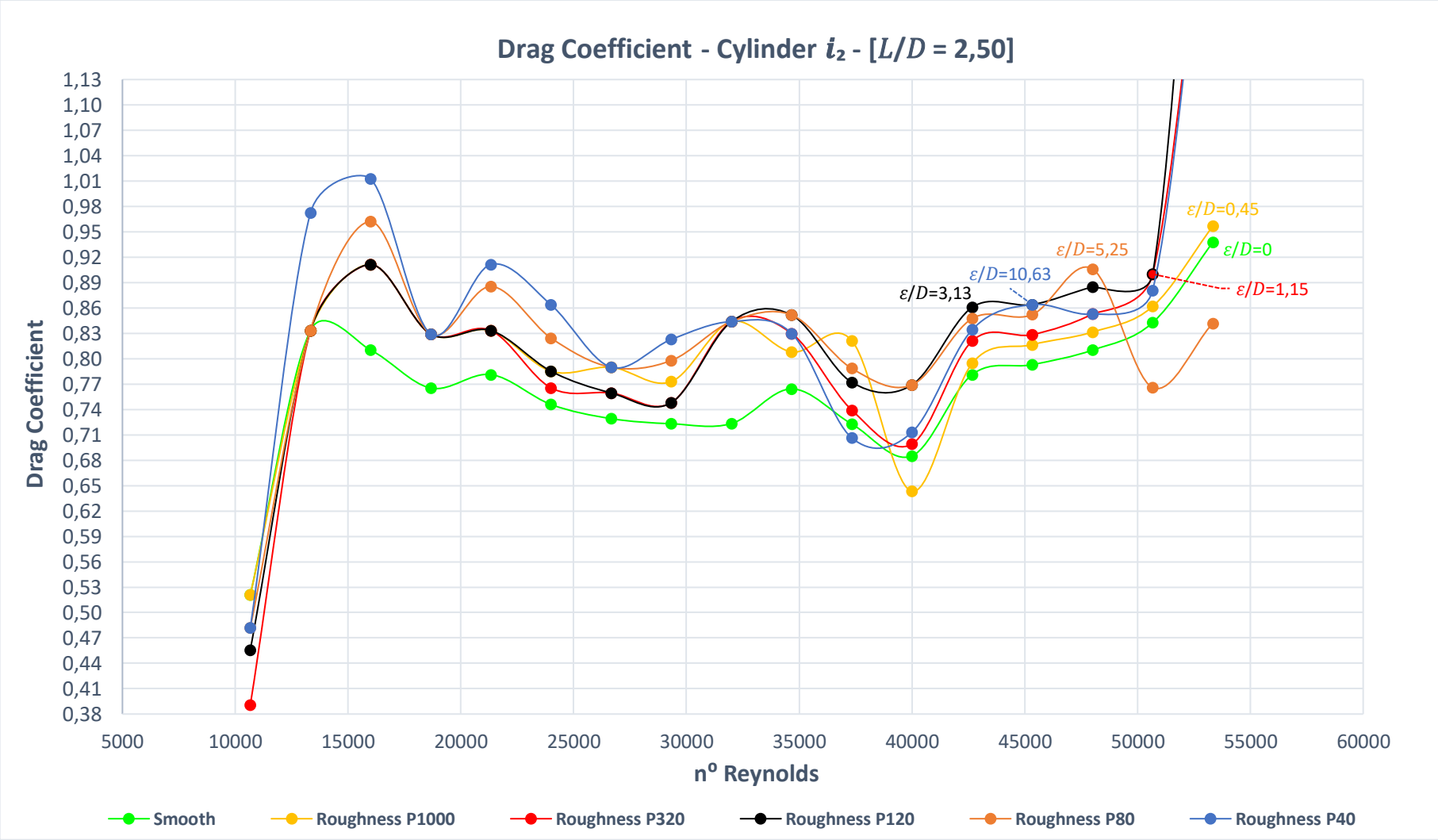

Figure 46. Comparative drag coefficients for cylinder i_2 considering the different relative roughness $\frac{\varepsilon}{D}$.

Chapter 5

Conclusion

Experimental simulations of engineering problems are great tools to help solve the complex study of external flows in a submerged body. In this work, the use of the wind tunnel allowed to simulate the external flows in cylinders, which made it possible to obtain drag forces relatively close to the expected. In spite of that, the same did not happen for the drag coefficients since they presented significant errors in relation to the theoretical value expected for a cylinder without roughness.

However, although significant differences were observed for drag coefficients, the experimental work allowed us to verify, at least qualitatively, the variation of these coefficients in relation to the Reynolds number range: fluctuation of the points around an average value, the which characterizes the typical constant pattern of the drag coefficients of cylinders in the interval,$1{,}1\ x\ 10^4 \leq Re \leq 5{,}3\ x\ 10^4$, whose greatest effects are preponderant of the pressure drag.

Compared to smooth cylinders, the insertion of surface roughness qualitatively evidenced that in fact similar variations occur in the behavior of drag coefficients. However, in the range $1{,}1\ x\ 10^4 \leq Re \leq 5{,}3\ x\ 10^4$Quantitative analysis is needed to reach a consensus on the variations revealed in the graphs. It is assumed with this, in future works, resort to a precise analysis in the collection of forces, also increasing the width of the Reynolds number range to obtain better clarity about the behavior of the drag coefficients against the inserted roughnesses.

In summary, the results of this work are considered reasonable, having fulfilled all the objectives. The fluctuation of the points revealed the presence of different sources of uncertainty, the effect of the vibration transmitted from the motor shaft to the measurement system being clearly perceptible and increasingly present as the flow velocities increased. This reflected the greatest uncertainties especially for the highest Reynolds number values in the study.

As future perspectives, the following considerations are suggested for improvement and continuity of the study:

- In the accuracy of the current measurement system, when studying the effects of roughness, it is suggested to insert even more prominent protrusions on the surface, as the measurement system will certainly be able to show significant differences.
- Study a project of a more accurate measurement system for the wind tunnel, in order to make possible conclusions about experiments that require less surface roughness.
- Design a damping for the experimental bench in order to cooperate in the complete isolation of the measuring system, thus avoiding the unwanted effect of mechanical vibrations.

Bibliographic References

[1] ANDERSON JR, J. D. Fundamentals of aerodynamics. 5th edition. The McGraw-Hill Companies, New York, NY, 2010. ISBN 978-0-07-339810-5.

[2] ÇENGEL, Y. A.; CIMBALA, J. M. Fluid Mechanics: Fundamentals and Applications. The McGraw-Hill Companies, New York, NY, 2006. ISBN 0-07-247236-7.

[3] EPIFANOV, V. M. Boundary Layer. Thermopedia. Available at < https://thermopedia.com/content/595/>. Access in 5 jun. 2021.

[4] WHITE, F. M. Fluid Mechanics. 7th edition. The McGraw-Hill Companies, New York, NY, 2011. ISBN 978-0-07-352934-9.

[5] POLYTECHNIC SCHOOL OF THE UNIVERSITY OF SÃO PAULO. Fluid Mechanics I Notes PME2230. Available at < http://sites.poli.usp.br/d/pme2230/Arquivos/Slides-EscoamentoExterno-pme2230-2013.pdf > Access in 6 jun.2021.

[6] SCHLICHTING, H.; GERSTEN, K. Boundary-Layer Theory. Physic and astronomy. Springer, 2000.

[7] MARYAMI, R.; SHOWKAT ALI, S. A.; AZARPEYVAND, M., & AFSHARI, A. Turbulent flow interaction with a circular cylinder. Physics of Fluids, 32(1), [015105 (2020)]. Available at < https://doi.org/10.1063/1.5119967 > Access in 10 jun. 2021.

[8] GOMES, F. V. Resistência hidrodinâmica de pilares cilíndricos hidraulicamente rugosos. Faculty of Engineering of the University of Porto. 1981. Available at < https://hdl.handle.net/10216/12363> Access in 14 jun. 2020.

[9] PRITCHARD, P.J; LEYLEGIAN J.C.; Fox and McDonald's Introduction to Fluid Mechanics. 8th edition. John Wiley & Sons, Inc.2011. ISBN 13 9780470547557 e ISBN-10 0470547553

[10] STEFANO, D.; IANIRO, A. Experimental Aerodynamics. CRC Press Taylor & Francis Group. 2017. ISBN 978-1-4987-0401-4.

[11] BARLOW, J. B.; RAE, W. H.; POPE, A. Low-speed Wind Tunnel Testing: 3rd edition. Wiley-Imterscience Publication. 1999.

[12] NATIONAL AERONAUTICS AND SPACE ADMINISTRATION. Wind Tunnel Theory. Available at: < https://www.grc.nasa.gov/www/k-12/airplane/tunnozt.html >. Access in 10 jun. 2021.

[13] NATIONAL AERONAUTICS AND SPACE ADMINISTRATION. Open Return Wind Tunnel. Available at: < https://www.grc.nasa.gov/WWW/k-12/airplane/tunoret.html>. Access in 10 jun. 2021

[14] NATIONAL AERONAUTICS AND SPACE ADMINISTRATION. Closed Return Wind Tunnel. Available at: < https://www.grc.nasa.gov/WWW/K-12/airplane/tuncret.html>. Access in: 10 jun. 2021.

[15] SCHALKWYK, J. Sometimes size does matter: 25 years with the largest wind tunnel in the world. Available at: < https://phys.org/news/2012-12-size-years-largest-tunnel-world.html >. Access in 8 jun. 2021.

[16] SIENCE BUDDIES. How to Build and Use a Subsonic Wind Tunnel. Available at: < https://www.sciencebuddies.org/science-fair-projects/references/how-to-build-a-wind-tunnel > Access in 8 jun. 2021.

[17] MACINTYRE, A. J. Equipamentos Industriais e de processo. LTC GEN. Rio de Janeiro. 2019. ISBN 978-85-216-1107-3

[18] VERSTEEG, H. K.; MALALASEKERA, W. An introduction to computational fluid dynamics: the finite volume method. Pearson Education, 2007.

[19] DAMBROZ, G. Obtenção de coeficientes aerodinâmicos em simulação computacional de escoamento externo. 2019. Available at < https://bibliodigital.unijui.edu.br:8443/xmlui/bitstream/handle/123456789/6041/Giovani%20Prates%20Bisso%20Dambroz.pdf?sequence=1&isAllowed=y > Access in 5 jun. 2021.

[20] SHARAN S. Flow Over a Cylinder. Available at < https://skill-lync.com/projects/flow-over-a-cylinder-149 >. Access in 9 June 2021.

[21] Federation of European Producers of Abrasives.

[22] ARMFIELD LIMITED. C2 - Túnel de vento subsônico. Disponível em: <https://armfield.co.uk/product/c2-subsonic-wind-tunnel/> > Access in 25 Jul. 2021.

[23] DIAS, V. Determination of The Drag Coefficient of an Autonomous Solar Lighting Column Using Wind Tunnel Simulation and Computational Analysis. Dissertation presented to Higher School of Technology and Management Polytechnic Institute of Bragança to obtain the master's degree at Industrial Engineering. 2019. Available at < https://bibliotecadigital.ipb.pt/handle/10198/20519 > Access in 30 jul. 2021

[24] PRAVATO, W. Estudo do arrasto aerodinâmico a partir de simulações em túnel de vento. Relatório final de Dissertação apresentado à Escola Superior de Tecnologia e Gestão para a obtenção do grau de Mestre em Engenharia Industrial. 2020. Available at < https://bibliotecadigital.ipb.pt/bitstream/10198/22679/1/pauta-relatorio-29.pdf > Access in 30 jul. 2021